Positron Emission Tomography: A Review of Basic Principles, Scanner Design and Performance, and Current Systems

Pat Zanzonico

SINCE THE INCEPTION of positron emission tomography (PET) several decades ago, PET scanner design and performance have improved dramatically. The number of detector elements has increased from ~20 to ~20,000 and the axial field of view from ~2 to ~ 20 cm, the spatial resolution has improved from ~25 to ~5 mm, and the sensitivity has increased ~1000-fold.[1,2] At the same time, the clinical applications of PET have grown dramatically as well.[3-5] The current article reviews the technical basis of the remarkable advance of this modality—the underlying principles of PET and the basic design and performance characteristics of PET scanners—emphasizing dedicated "full-ring" devices and including multimodality (ie, PET-CT) and special-purpose (ie, small-animal) devices.

PHYSICAL BASIS OF PET AND PET "EVENTS"

PET is based on the annihilation coincidence detection (ACD) of the two colinear 511-keV γ-rays resulting from the mutual annihilation of a positron and a negatron, its antiparticle (Fig 1). Positron-negatron annihilation occurs at the end of the positron range, when the positron has dissipated all of its kinetic energy and both the positron and negatron are essentially at rest. The *total* positron and negatron energy is therefore 1.22 MeV, the sum of their equal rest mass energies (E_o = 511, keV = 0.511 MeV), and their *total* momentum (a vector, or signed, quantity) is zero. Accordingly, to conserve energy and momentum, the total energy of the two annihilation γ-rays must equal 1.22 MeV and their total momentum zero. Two equal-energy (511-keV) annihilation γ-rays traveling in opposite directions, corresponding to equal-magnitude, opposite-sign (positive and negative) momenta, are therefore emitted.

In the parlance of ACD, each of the two annihilation photons is referred to as a "single" and the total count rate (counts per second (cps)) for the individual annihilation photons is called the "singles count rate" (Fig 1). Only when signals from the two coincidence detectors simultaneously trigger the coincidence circuit is an output, a "true coincidence event" ("true"), generated by this circuit. The volume between the opposed coincidence detectors (the shaded area in Fig 1) is referred to as a "line of response (LOR)." LORs are thus defined electronically, and an important advantage of ACD is that absorptive collimation is not required. As a result, the sensitivity (measured count rate per unit activity) of PET is much higher (two to three orders of magnitude higher) than that of Anger camera imaging.[6] Not every annihilation yields a counted event, however, because *both* annihilation photons must strike the coincident detectors for an event to be counted. As a result, the singles count rate in PET is typically much higher than the trues count rate.

The 511 keV-in-energy and the simultaneity-of-detection requirements for counting of a true coincidence event are not absolute. Scintillation detectors typically have a rather coarse energy resolution—up to ~30% (expressed as the percent full-width half-maximum of the 511-keV photopeak)—and therefore photons within a broad energy range (eg, 250 to 650 keV) can be counted as valid annihilation γ-rays.[7] Compton-scattered annihilation γ-rays and scattered and unscattered nonannihilation photons may therefore be included, producing spurious or mispositioned coincidence events.

Each detected photon (single) is time-stamped ($\pm$1 ns = 1×10^{-9} s), and a true coincidence event is defined as a pair of annihilation photons counted by the coincidence detectors within a time interval called the "coincidence timing window τ," typically 6 to 12 ns. Such a finite timing window is necessitated by several considerations. First, depending on the exact position of the positron-negatron annihilation, the annihilation photons reach the detectors at slightly different times. However, because these photons travel at the speed of light ($c = 3 \times 10^{10}$ cm/s), this effect is very small. Second, the transit and processing of the signal pulses through the detector circuitry is rapid

From the Memorial Sloan-Kettering Cancer Center, New York, NY.

Address reprint requests to Pat Zanzonico, PhD, Memorial Sloan-Kettering Cancer Center, 1275 York Avenue, New York, NY 10021.

0001-2998/04/3402-0003$30.00/0

doi:10.1053/j.semnuclmed.2003.12.002

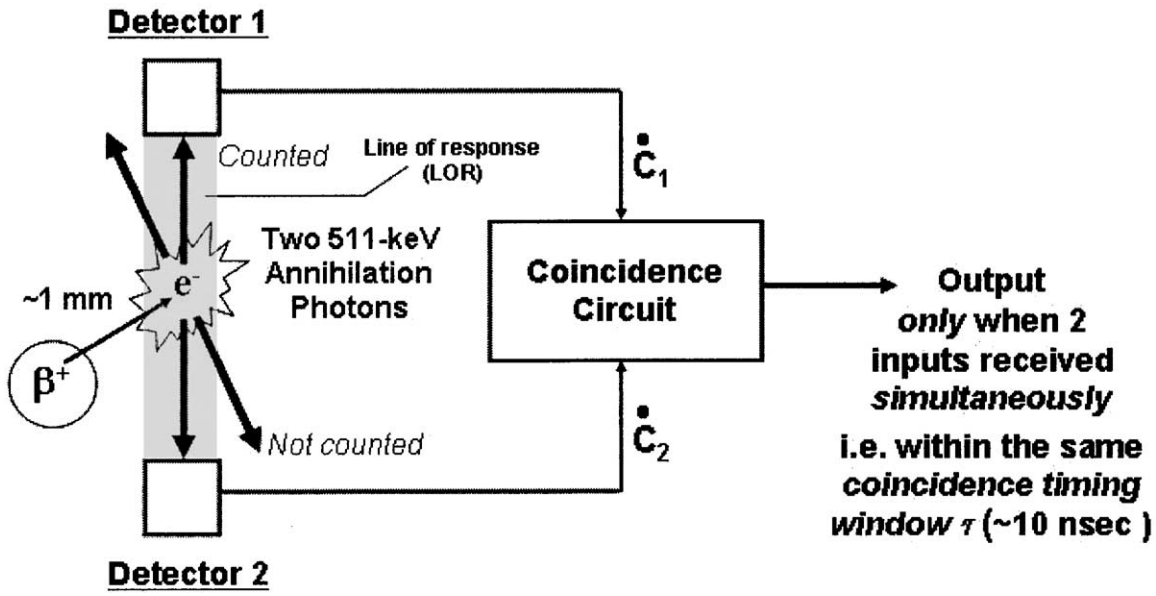

Fig 1. The basic principle of ACD. An event is counted only when each of the two 511-keV annihilation γ-rays are detected simultaneously, that is, within a time interval corresponding to the coincidence timing window τ, by the two detectors. The shaded LOR corresponds to the volume between and defined by the cross-sectional area of the coincidence detectors 1 and 2 and $\dot{C}_1$ and $\dot{C}_2$ are the singles count rates recorded by detectors 1 and 2, respectively.

but not instantaneous. Third, the light signal emitted by the scintillation detectors used in PET is emitted not instantaneously but over a finite time interval, called the "scintillation decay time," of the order of 10 to 100 ns.

In addition to the true coincidence events (Figs 1 and 2A), a number of other types of events occur in PET, events that degrade quantitative accuracy as well as image quality. Random or accidental coincidence events ("randoms") occur when annihilation γ-rays from two separate positron-negatron annihilations are detected in two different detectors within the coincidence timing window τ (Fig 2B). Randoms thus increase the detected coincidence count rate by contributing spuriously placed coincidence events. Because the total activity-containing volume is typically much greater than the LOR, random coincidences are common and the randoms count rate may actually exceed the trues count rate. Clinically, the ratio of the randoms-to-true count rates range from 0.1 to 0.2 for brain imaging to greater than 1 for whole-body imaging.[6]

The randoms count rate is actually proportional to the product of the singles count rate and therefore the square of the activity present[6]:

$$\dot{C}_{\text{randoms}} = 2\tau\dot{C}_1\dot{C}_2 \qquad (1)$$

where $\dot{C}_{\text{randoms}}$ = the randoms count rate (cps), τ = the coincidence timing window (sec), and $\dot{C}_1$ and $\dot{C}_2$ = the detector 1 and detector 2 singles count rates (cps), respectively (Fig 1). Importantly, because the trues count rate is only linearly proportional to the activity, the ratio of the randoms-to-trues count rates increases linearly with activity. Therefore, imaging times cannot be reduced simply by using higher and higher administered activities, as the randoms count rate will increase more rapidly than the trues count rate and at some point prohibitively degrade image quality. By using absorptive septa to restrict the activity-containing region sampled by coincidence detectors to a volume defined by the cross-sectional area of the detectors—as in two-dimensional (2D) PET (see below)—the randoms-to-true count rate ratio can be reduced substantially. By using "faster" detectors and therefore shorter coincidence timing windows, the randoms-to-true count rate can be reduced further (see below).

Annihilation γ-rays traveling out of an LOR may undergo Compton scatter and be re-directed back into the LOR (Fig 2C). The scattered photon may, however, retain sufficient energy to fall within the energy window set for the 511-keV annihilation γ-rays and produce a coincidence

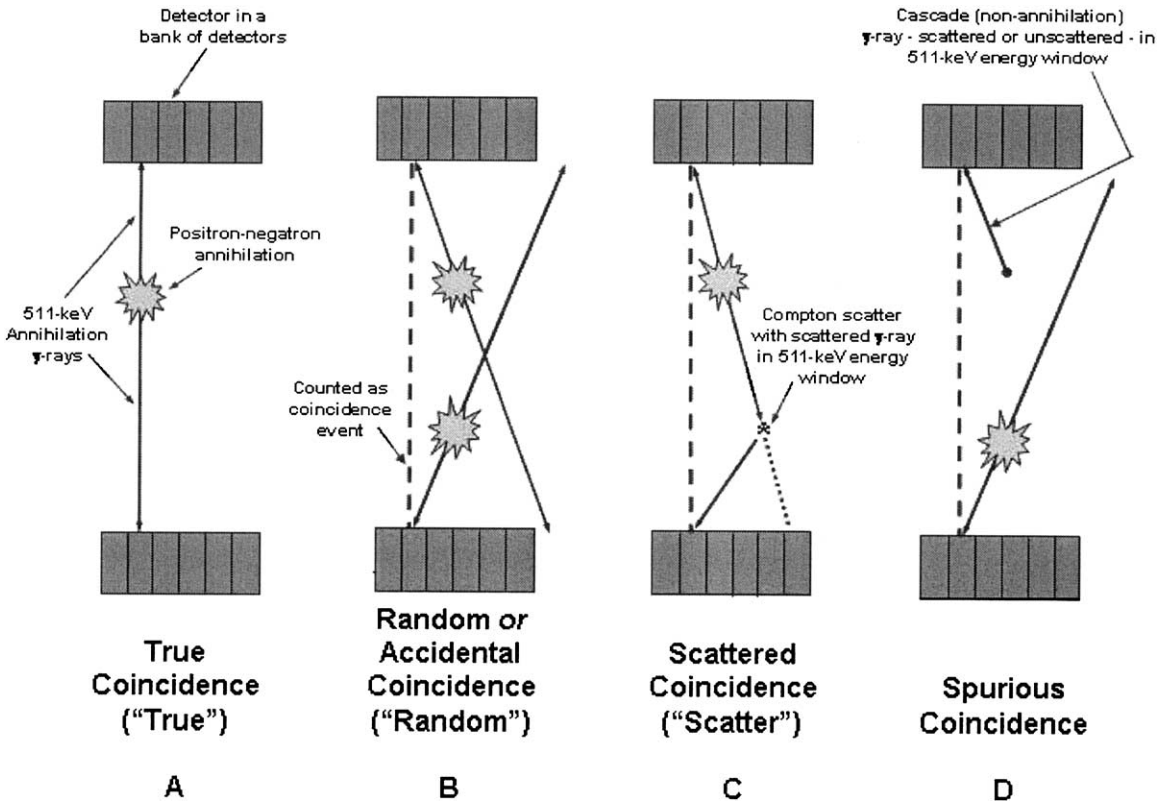

Fig 2. The various events associated with ACD of positron-emitting radionuclides, illustrated for two opposed banks of coincidence detectors and assuming only one opposed pair of detectors are in coincidence. (A) A true coincidence ("true") is counted only when each of the two 511-keV annihilation γ-rays for a single positron-negatron annihilation are not scattered and are detected within the timing window τ of the two coincidence detectors. (B) A random or accidental coincidence ("random") is an inappropriately detected and positioned coincidence (the dashed line) that arises from two separate annihilations, with one γ-ray from each of the two annihilations detected within the timing window τ of the coincidence-detector pair. (C) A scattered coincidence ("scatter") is a mispositioned coincidence (the dashed line) resulting from a single annihilation, with one of the γ-rays undergoing a small-angle Compton scatter but retaining sufficient energy to fall within the 511-keV energy window. (D) A spurious coincidence is an inappropriately detected and positioned coincidence (the dashed line) which arises from an annihilation and a cascade γ-ray, scattered or unscattered but having sufficient energy to fall within the 511-keV energy window. Spurious coincidences occur only for radionuclides which emit both positron and prompt cascade γ-ray(s).

event. Such scatter coincidences ("scatter") result in mispositioned events. The scatter count rate as well as the trues count rate are proportional to the activity present and therefore the scatter-to-trues count rate ratio is independent of activity.[6] Because trues and scatter each result from single annihilation events, the scatter-to-trues count rate ratio is likewise independent of the coincidence timing window. On the other hand, interdetector septa used in 2D PET (See below.) reduce the scatter count rate considerably.

Many positron-emitting radioisotopes also emit significant numbers of high-energy prompt γ-rays, and such γ-rays may be in cascade with each other or with the positrons.[8,9] These can result in spurious coincidences which are spatially uncorrelated but nonetheless counted as true events (Fig 2D).[10,11] Although such coincidences degrade overall quality and quantitative accuracy, isotopes such as have copper-62, gallium-66, gallium-68, bromine-75, rubidium-82, yttrium-86, and iodine-124, nonetheless been used effectively in PET.[10,11] Table 1 includes, for selected positron emitters, the energy and abundance of γ- (and x-) rays with sufficient energy (ie, greater than 250 keV) to fall within the 511-keV energy windows typically used to count annihilation γ-rays in PET. Besides the γ-ray energies and abundance, Table 1 includes other pertinent properties of positron emitters such as the physical half-life ($T_{1/2}$), the branching ratio (ie, the percentage of total decays resulting in positron emission instead of electron capture), the

Table 1. Physical Properties of Positron-Emitting Radionuclides Used in PET[8,9]

Radionuclide	Physical Half-life $T_{1/2}$	Branching Ratio	Maximum $\beta+$ Energy (MeV)	$\beta+$ Range in Water (mm)		x- and γ-rays >0.25 MeV		Production
				R_e (ref. 75)	R_{rms} (ref. 24)	Energy (MeV)	Abundance	
Carbon-11	20.4 min	99%	0.96	3.9	0.4	N/A	0%	Cyclotron
Nitrogen-13	9.96 min	100%	1.2	5.1	0.6	N/A	0%	Cyclotron
Oxygen-15	2.05 min	100%	1.7	8.0	0.9	N/A	0%	Cyclotron
Fluorine-18	1.83 h	97%	0.64	2.3	0.2	N/A	0%	Cyclotron
Copper-62	9.74 min	98%	2.9	15	1.6	0.876-1.17	0.5%	Generator (Zinc-62)
Copper-64	12.7 h	19%	0.58	2.0	0.2	N/A	0%	Cyclotron
Gallium-66	9.49 h	56%	3.8	20	3.3	0.834-4.81	73%	Cyclotron
Gallium-68	1.14 h	88%	1.9	9.0	1.2	1.08-1.88	3.1%	Generator (Germanium-68)
Bromine-76	16.1 h	54%	3.7	19	3.2	0.473-3.60	146%	Cyclotron
Rubidium-82	1.3 min	95%	3.4	18	2.6	0.777	13%	Generator (Strontium-82)
Yttrium-86	14.7 h	32%	1.4	6.0	0.7	0.440-1,920	240%	Cyclotron
Iodine-124	4.18 d	22%	1.5	7.0	0.8	0.603-1,690	23%	Cyclotron

maximum positron energies (E_{max}), the maximum extrapolated range (R_{max}), the root-mean-square (rms) positron range (R_{rms}), and the method of production.

PET DETECTORS AND DETECTOR CONFIGURATIONS

Detector Materials

To date, only four detector materials—all inorganic scintillators—have been widely used in PET scanners: thallium-doped sodium iodide (NaI(Tl)), bismuth germanate (BGO), cerium-doped lutetium oxyorthosilicate (LSO(Ce) or simply LSO), and cerium-doped gadolinium oxyorthosilicate (GSO(Ce) or simply GSO) (Table 2).[7,12,13]

The most important practical features of scintillation detectors include high mass density (ρ) and effective atomic number (Z_{eff}), high light output, and speed (Table 2). A high mass number and high effective atomic number maximize the crystal stopping power (ie, linear attenuation coefficient μ) and therefore the detection of radiations. In addition, a higher-atomic number crystal will have a higher proportion of photoelectric than Compton interactions,[7] facilitating energy discrimination of scattered photons. High light output reduces statistical uncertainty (noise) in the scintillation and associated electronic signal and thus improves energy resolution and scatter rejection. A fast crystal (ie, a crystal with a short scintillation decay time) allows the use of a narrow coincidence timing window, τ, reducing the randoms count rate. Other detector considerations include: transparency of the crystal to its own scintillations (ie, minimal self-absorption); matching of the index of refraction (η) of the crystal to that of the photodetector (specifically, the entrance window [$\eta \approx 1.5$] of a photomultiplier tube [PMT]); matching of the scintillation wavelength to the light response of the photodetector (the PMT photocathode, with maximum sensitivity in the 390-410 nm, or blue, wavelength range); and minimal hygroscopic behavior.[7]

NaI(Tl) crystals were used in the original PET scanners. Higher-density and -effective atomic materials, such as BGO, LSO, and GSO, have emerged as the detectors of choice for PET because of their greater stopping power for 511-keV annihilation γ-rays (Table 2). Note, for example, that the attenuation length for 511-keV γ-rays is at least twice as long in NaI(Tl) as in BGO, GSO, or LSO. Among the latter three materials, GSO and LSO have a faster light output—nearly 10-fold faster—than BGO, with LSO having a much greater light output—approximately 3-fold greater—than either BGO or GSO. GSO has somewhat better energy resolution, and scatter rejection capability, than either BGO or LSO.

A notable disadvantage of LSO is the presence of a naturally-occurring long-lived radioisotope of lutetium, lutetium-177.[7] Lutetium-177 has an isotopic abundance of 2.6% and a half-life of $\sim 4 \times 10^{10}$ years and emits two prompt γ-rays (88% abundance) of 201 and 306 keV in energy; the summed energy of 507 keV falls well within the 511-keV energy windows commonly used in PET scanners. The presence of lutetium-177 results in a measured background count rate of 240 cps/cm^3 of

LSO[14] and singles and trues count rates of 100,000 and 10,000 cps, respectively, in clinical LSO PET scanners. Although the former has a negligible effect on typical emission scans, the latter would significantly increase the statistical uncertainty (noise) in single-photon transmission scans (eg, with cesium-137) used for attenuation correction.[7]

Detector Configurations

Most commonly in dedicated PET scanners, detectors are arranged in rings or polygonal arrays of discrete, small-area detectors completely encircling the patient (Figs 3A–C). In such systems, multi-coincidence fanbeam detection is used, with each detector element operated in coincidence with multiple opposed detector elements. For a ring comprised of N detector elements, a total of N/4 to N/2 fanbeams is acquired. In rings, each element is typically in coincidence with about half of the total detectors in the ring and in polygonal arrays with the opposed detector bank. PET systems with only partial detector rings are less expensive but require rotation of the detector assembly about the longitudinal axis of the patient to complete acquisition of the projection data (Fig 3B). In addition, continuous, large-area detectors, such as those found in multi-head Anger camera systems and used for single-photon emission computed tomography (SPECT), have now been appropriately modified and are used for coincidence imaging of positron emitters (Fig 3D). With two or even three such detectors, rotation (180 or 120°, respectively) is required for complete angular sampling. Alternatively, large-area detectors may be arranged in a polygon (if flat) or in a circle (if curved) completely encircling the patient (Fig 3E and F); such systems have been manufactured using GSO as well as NaI(Tl).

Technical performance improves but cost increases as one progresses from dual-head coincidence Anger cameras at the low end to partial rings to polygonal arrays to multiple full rings at the high end—multiple rings being the prevailing configuration among current dedicated PET scanners.[2] Clinical performance, specifically, lesion detectability improves as well, as demonstrated in a study by Kadrmas and Christian[15] using a realistic whole-body anthropomorphic phantom with multiple focal lesions with clinically realistic dimensions and lesion-to-background activity concentration ratios. Lesion detectability was clearly best

Table 2. Physical Properties of PET Scintillators[7]

Material	Composition	Density, ρ (gm/cm^3)	Effective Atomic Number, Z_{eff}	Linear Attenuation Coefficient, μ, for 511-keV γ-rays (/cm)	Relative Probability of Photoelectric Interaction (%)	Light Output (photons per MeV)	Scintillation Decay Time (nsec)	Scintillation wavelength, λ (nm)	Energy Resolution at 511 keV (% FWHM)	Hygroscopic (Y/N)?	Refractive Index, η
Bismuth Germanate BGO	$Bi_4Ge_3O_{12}$	7.1	75	0.95 ϵ^2 (2 cm) = 0.72*	40	9,000	300	480	12	N	2.15
Gadolinium Oxyorthosilicate GSO	Gd_2SiO_5: Ce	6.7	59	0.70 ϵ^2 (2 cm) = 0.57*	25	8,000	60	440	9	N	1.85
Lutetium Oxyorthosilicate LSO	Lu_2SiO_5:Ce	7.4	66	0.88 ϵ^2 (2 cm) = 0.69*	32	30,000	40	420	10	N	1.82
Sodium Iodide NaI(Tl)	NaI:Tl	3.7	51	0.34 ϵ^2 (2 cm) = 0.24*	17	41,000	230	410	8	Y	1.85

*The intrinsic efficiency of 2-cm thick coincidence detectors for 511-keV annihilation γ-rays.

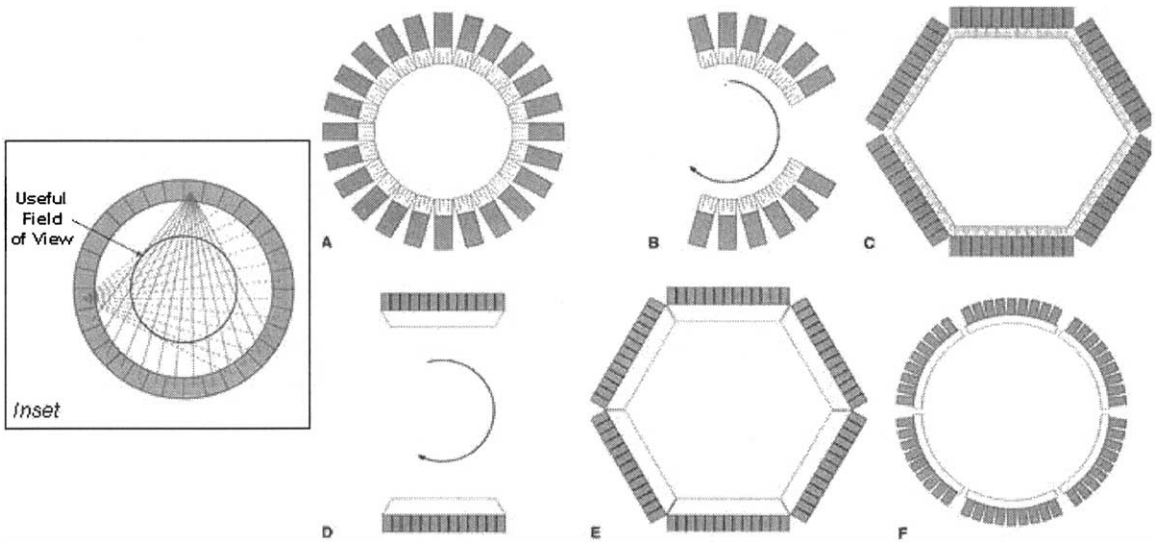

Fig 3. PET scanner detector configurations. (A) Multiple full rings of detector blocks comprised of discrete, small-area detector elements. (B) Multiple partial rings of detector blocks comprised of small-area detector elements. (C) Hexagonal array of detectors banks comprised of small-area detector elements. (D) Opposed large-area detectors such as Anger cameras. (E) Hexagonal array of large-area detectors. (F) Circular arrangement of six large-area, curved detectors. *Inset:* Multi-coincidence fanbeam detection used in detector rings and arrays of small-area detectors. Such fanbeam transverse sampling data are generally treated as parallel-beam data. Adapted from Cherry et al[6] with permission.

among the multiple-ring systems and poorest among coincidence Anger camera systems, with the most pronounced differences for the smallest lesions (Fig 4).

Early PET detectors consisted of a single scintillation crystal backed by a single PMT, with the cross-sectional dimensions of the crystal defining the coincidence LOR and thus intrinsic (ie, crystal) spatial resolution. To improve spatial resolution, therefore, greater numbers of smaller crystals are required. Thus, the practically achievable miniaturization of PMTs and associated electronics and the cost of large numbers of detectors, PMTs, etc, representing well over half of the costs of PET scanners,[16] limit intrinsic resolution. The block detector[1,2,17] was an ingenious solution to this limitation.

A block detector consists of a large cubic piece of scintillator (2 × 2 to 3 × 3 cm in cross section by 2 to 3 cm in depth) partially cut, or scored, depth-wise into a rectangular array of detector elements (Fig 5A). The cuts are filled with reflective material to optically isolate the detector elements from one another and to maximize light collection efficiency by the PMTs backing the scintillator. Crystal elements with a somewhat smaller cross-section improve spatial resolution—but only to a certain point. As the cross-section of detector elements is reduced and the number of elements increased, the number of cuts and therefore the fraction of the scintillator face occupied by the filling material increase. As a result, the detector element packing fraction (ie, the fraction of the scintillator face occupied by scintillation material) and therefore the intrinsic sensitivity decrease.

The depth of the cuts into the crystal is not uniform but increases from approximately half the thickness at the center to nearly the full thickness at the edge of each side of the scintillator (Fig 5A); the actual depths of the cuts are determined empirically to yield a spatially linear distribution of light among the four PMTs—in a 2 × 2 array—backing the scintillator. The position at which the annihilation γ-ray strikes the scintillator is then determined by Anger arithmetic. The response of the block detector is not uniform (Fig 5B). Rather, recorded events are clustered at points corresponding to the individual detector elements and then assigned to a specific element in the two-dimensional array using a look-up table derived by uniform irradiation of the scintillator. The major advantage of the block detector is that it allows an array of many small detector elements (typically 8 × 8 = 64) to be spatially encoded using only

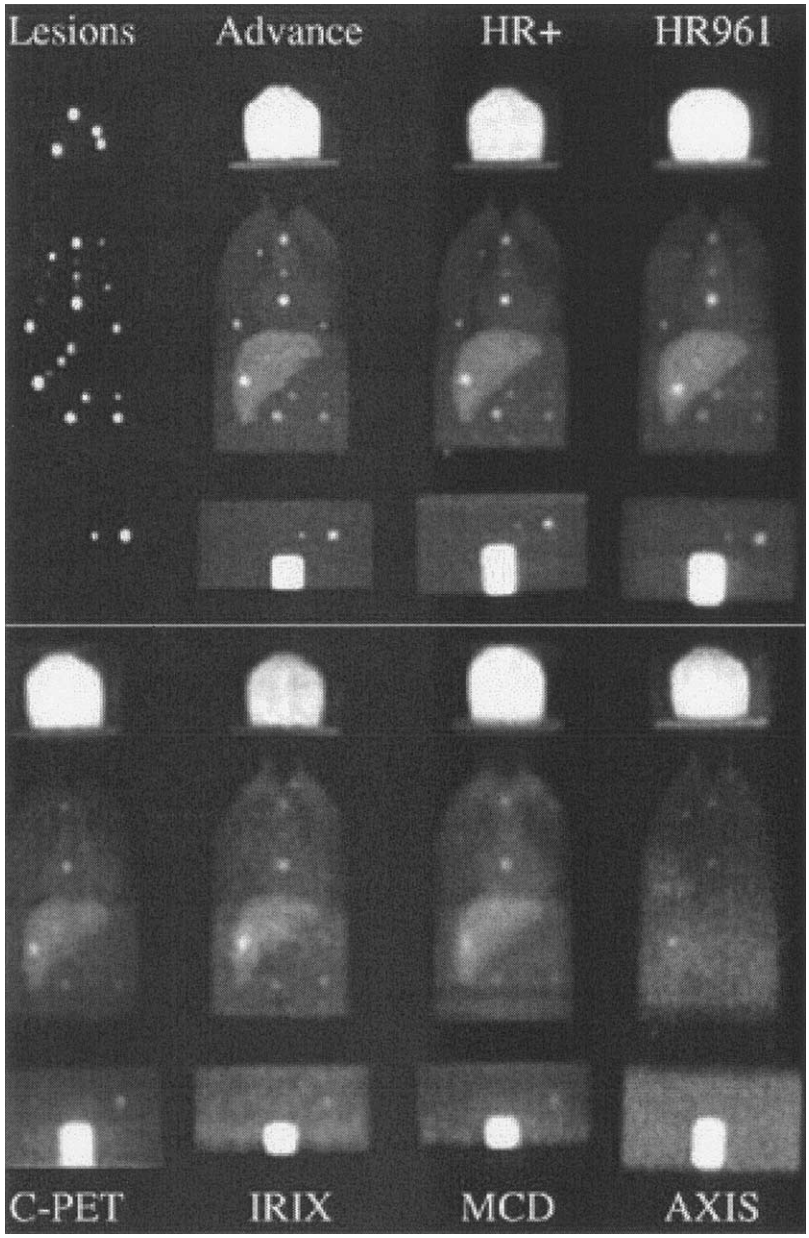

Fig 4. Comparative coronal images, obtained with seven commercially available systems, of a whole-body anthropomorphic phantom with 27 focal lesions filled with the positron-emitter sodium-22. The lesions were lucite spheres of inner diameters 7, 8, 12, and 16 mm and volumes 0.17, 0.27, 0.91, and 2.10 mL, respectively, and were filled with activity concentrations 4, 6, 10, and 16 times that in the background soft tissues. The total activity in the phantom at the start of each scan was 3 mCi. The systems evaluated included: three BGO dedicated full-ring PET scanners, the Advance (General Electric), the ECAT EXACT HR+ (Siemens-CTI, Knoxville, TN), and the ECAT EXACT HR961 (Siemens-CTI); a NaI(Tl) dedicated PET scanner with six large-area curved crystals, the C-PET (Philips-ADAC, Milpitas, CA); two NaI(Tl) hybrid PET-SPECT scanners with two Anger cameras, the Irix (Marconi Medical Systems, Cleveland, OH) and the Vertex MCD (Philips-ADAC); and a NaI(Tl) hybrid PET-SPECT scanner with three Anger cameras, the Axis (Marconi Medical Systems). Data were processed using the manufacturer-supplied software with manufacturer-suggested default processing parameters. Lesion detectability performance was clearly best among the BGO systems and poorest among the hybrid PET-SPECT systems. Reproduced from Kadrmas and Christian[15] with permission.

four PMTs rather than one PMT per element, yielding high spatial resolution while minimizing costs.

In modern ring-detector PET scanners (Table 2),[7,16] there are typically three to four rings of 100 to 200 block detectors each. There are about 6 to 8 cuts per block detector, yielding an array of $6 \times 6 = 36$ to $8 \times 8 = 64$ elements 4×4 to 6×6 mm each. Overall, therefore, there are a total of 10,000 to 20,000 detector elements. Ring diameters range from 80 to 90 cm, the patient ports and transaxial fields of view from 50 to 70 cm, and the axial (or longitudinal) fields of view from 20 to 30 cm, typically yielding about 50 transaxial image planes each 2 to 4 mm thick.

An important refinement of the block detector is "quadrant (or light) sharing,[6]" where a two-by-two array of four larger PMTs not only backs a single scintillator block but each PMT in the array also backs the corner of an adjacent block (Fig 5C). This reduces the total number of PMTs by a factor of four and thus reduces overall cost. Disadvan-

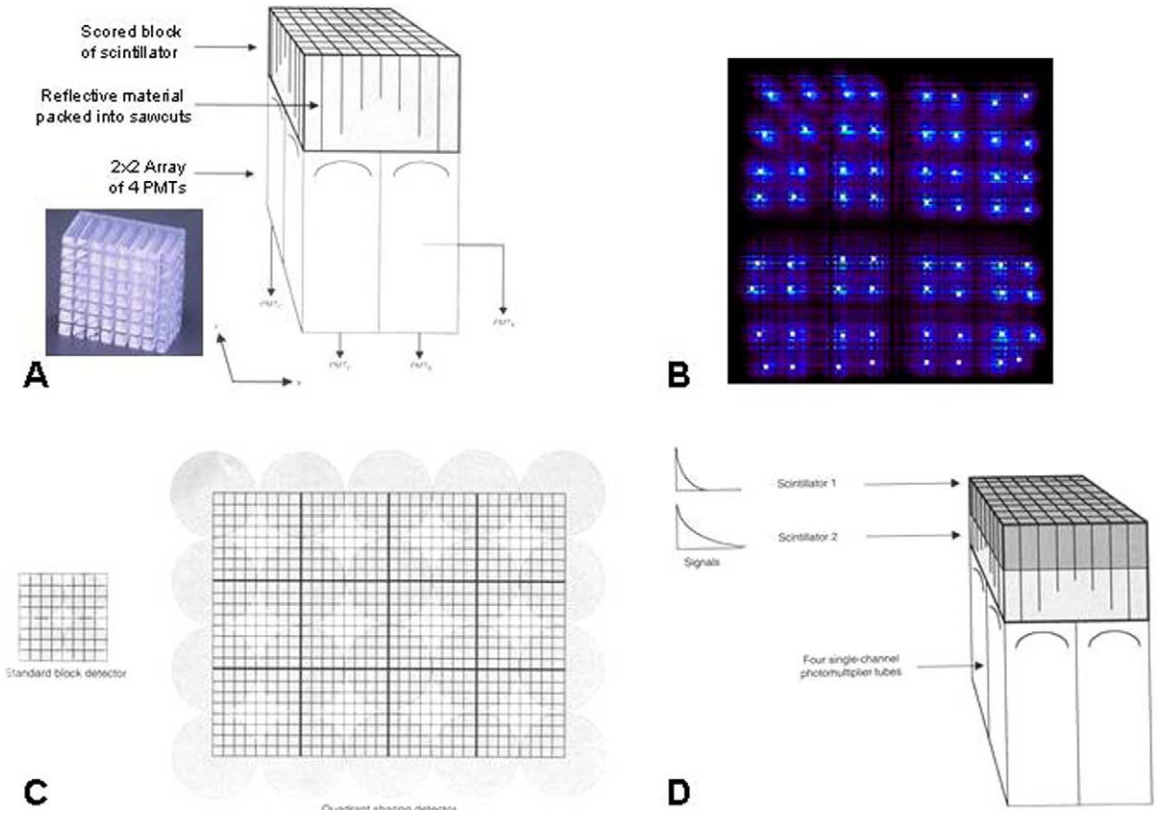

Fig 5. (A) Diagram of a typical block detector composed of a partially and variably scored scintillator crystal (photo) coupled to a 2 × 2 array of PMTs. (B) "Uncorrected" block detector image of a uniform radiation source. The detector response is nonuniform, with the recorded events clustered at points corresponding to the individual detector elements. (C) Arrangement of PMTs in a standard and in a quadrant-sharing block detector. In a standard block detector, a 2 × 2 array of PMTs backs a single scintillator crystal. In a quadrant-sharing block detector, each PMT in the 2 × 2 array backs the corners (or quadrants) in adjacent crystals. (D) Diagram of a phoswich block detector, comprised of adjacent layers of two materials with different scintillation decay times. Adapted from Cherry et al[6] with permission. (Color version of figure is available online.)

tages of quadrant sharing include higher deadtime count losses and more involved detector servicing because of the nonmodular design.

A notable refinement of PET scintillators has been the use of adjacent layers of two different materials with significantly different scintillation decay times (such as LSO and GSO, with decay times of approximately 40 and 60 nsec, respectively); this is known as phoswich (Fig 5D).[6] Based on the pulse shape of the scintillation signal, the interaction of the annihilation γ-ray can therefore be localized to one or the other half of the phoswich detector. The resolution-degrading depth-of-interaction effect is therefore reduced by a factor of two. However, the fabrication of phoswich is more complex than that of single-component detectors, and to date it has not been widely used in commercial PET scanners.

A recently developed alternative to the block detector is the pixelated detector matrix,[6,16,18] wherein individual small-area detectors elements (typically 4 × 6 mm in cross-section by 20 mm in depth) are fixed onto a continuous light guide backed by a close-packed array of PMTs (Fig 6). Pixelated detectors (PIXELAR™) are used in the Philips-ADAC (Milpitas, CA) Allegro PET scanner and Gemini PET-CT scanners.

Two-Dimensional (2D) Versus Three-Dimensional (3D) Data Acquisition

PET ring scanners originally employed lead or tungsten walls, or septa, positioned between and extending radially inward from the detector elements (Figs 7A–C). The Advance PET scanner (General Electric Medical Systems, Milwaukee, WI), for example, uses tungsten septa 1 mm thick and 12 cm long. In this approach, known as 2D PET, these interring annular septa define plane-by-

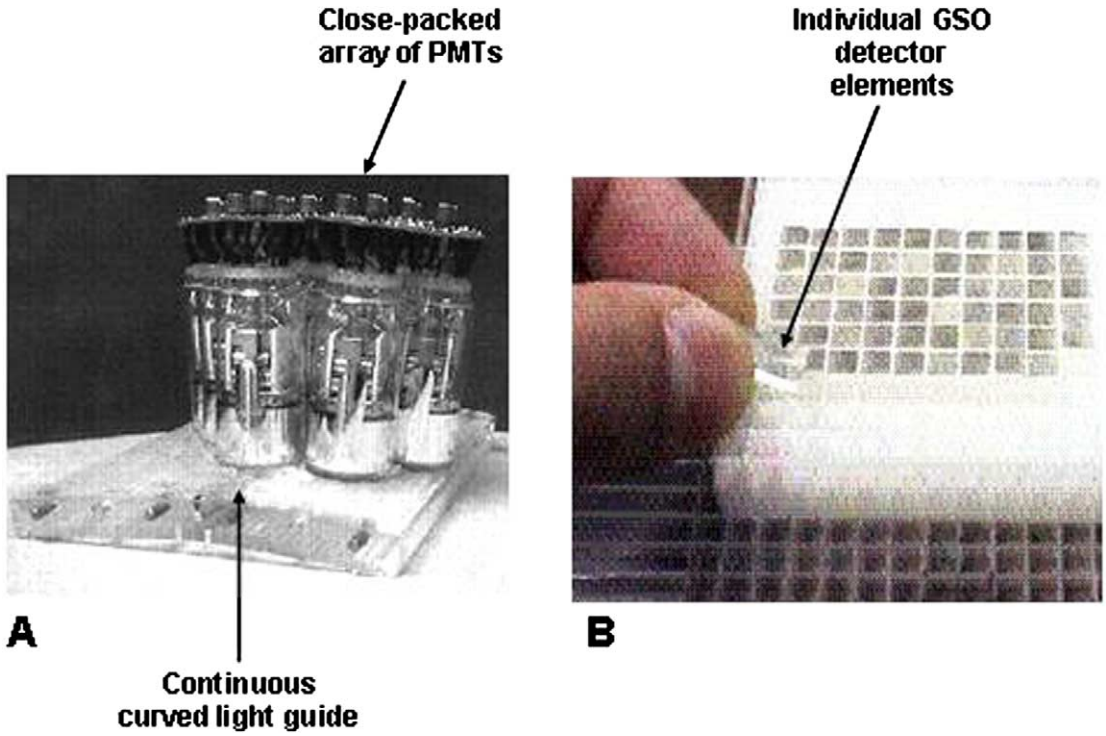

Fig 6. The Pixelar™ (Philips-ADAC) pixelated GSO detector, comprised of individual small-area detectors elements (A) fixed onto a continuous light guide backed by a close-packed array of PMTs (B). (Color version of figure is available online.)

plane LORs and largely eliminate out-of-plane annihilation γ-rays. By minimizing the contribution of out-of-plane randoms and scatter, image quality is optimized, especially for large-volume sources (ie, as in whole-body PET). However, 2D PET also eliminates most trues and thus reduces sensitivity considerably. Typically, both "direct" and "cross" image planes are reconstructed from LORs within the same detector ring (corresponding to a so-called "ring difference (Δ)" of 0) and between two adjacent detector rings (ring difference of ± 1), respectively. In the EXACT HR + 2D (Siemens-CTI) PET scanner, for example, 32 detector rings span an axial field of view (FOV) of 15.5 cm, yielding a total of 63 contiguous image planes comprised of 32 direct and 31 cross planes; in general, a scanner with n rings of detector elements yields a total of (2n − 1) image planes. The cross-planes lie halfway between the direct planes defined by detector elements and, conceptually, can be assigned to a "virtual" ring of detectors lying midway between two adjacent detector rings. Because the cross-plane images result from two LORs and the direct-plane images from only one, the cross-plane image sensitivity is about twice that of the direct-plane images (Figs 5A–C). This results, in an uncorrected PET study of a uniform volume source, in alternating lower-count and higher-count transverse section images. In the newer 2D PET systems, LORs among as many as three adjacent rings, corresponding to a ring difference of ± 3, are used to improve sensitivity. Increasing the ring difference does, however, degrade spatial resolution somewhat.

Sensitivity can be increased substantially by removing the septa altogether and including coincidence events from all of the LORs among all the detectors (Fig 7D)—a system with ~10,000 detector elements has approximately 100 million LORs. This is known as three-dimensional (3D) PET,[19] and is widely used among state-of-the-art PET scanners. ("Collimator-less" Anger camera-based coincidence imaging of positron emitters is inherently 3D.) Sensitivity is increased approximately fivefold in 3D relative to 2D PET—but with a considerable increase in the randoms and scatter count rates. Clinically, the scatter-to-true count rate ratios range from 0.2 (2D) to 0.5 (3D) in brain and from 0.4 (2D) to 2 (3D) in the whole body.[6] To compensate for the increase in scatter count rates,

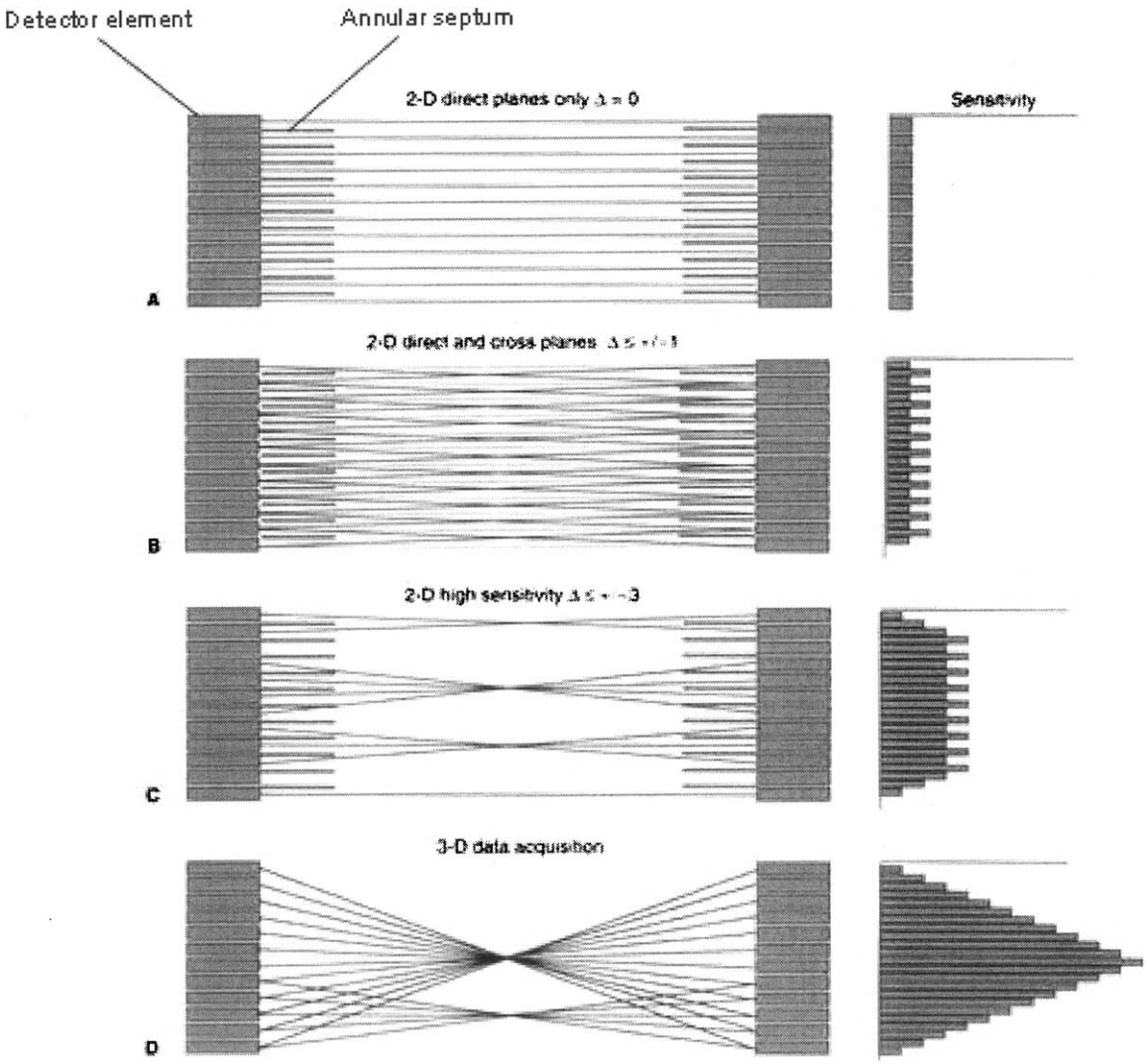

Fig 7. 2D and 3D PET data acquisition schemes (axial cross-sectional views of a multi-ring scanner) and the corresponding axial sensitivity profiles. (A–C) 2D data acquisition with a ring difference Δ of 0 (direct planes only), 1, and 3, respectively. (D) 3D (septa-less) data acquisition. The sensitivity profiles show the nonuniformity of response as a function of position along the axial FOV. Adapted from Cherry et al[6] with permission.

detectors (such as GSO and LSO) with better energy resolution[7] and accurate scatter-correction algorithms[20] are required for 3D PET. And, to minimize the increased randoms count rates and deadtime count-rate losses, shorter coincidence timing windows, and therefore faster detectors (such as GSO and LSO), are required. Data processing time, for 3D PET is about an order of magnitude longer than for 2D PET.[16,20]

In contrast to the relatively uniform axial sensitivity for 2D PET, the axial sensitivity profile for a 3D PET scanner is triangular and peaked at the center of the field of view (Fig 7D). Thus, whole-body 3D PET studies require considerable overlap of adjacent bed-position acquisitions—optimally, one-half of the axial FOVs[16,20]—to yield uniform sensitivity over the resulting whole-body images.

In PET in general and 3D PET in particular, it is important that the ends of the detector assembly are adequately shielded to minimize the contribution of counts from activity outside the axial FOV.

PET PERFORMANCE

An extensive series of parameters have been developed over the years to characterize PET scanner performance, and detailed data acquisition

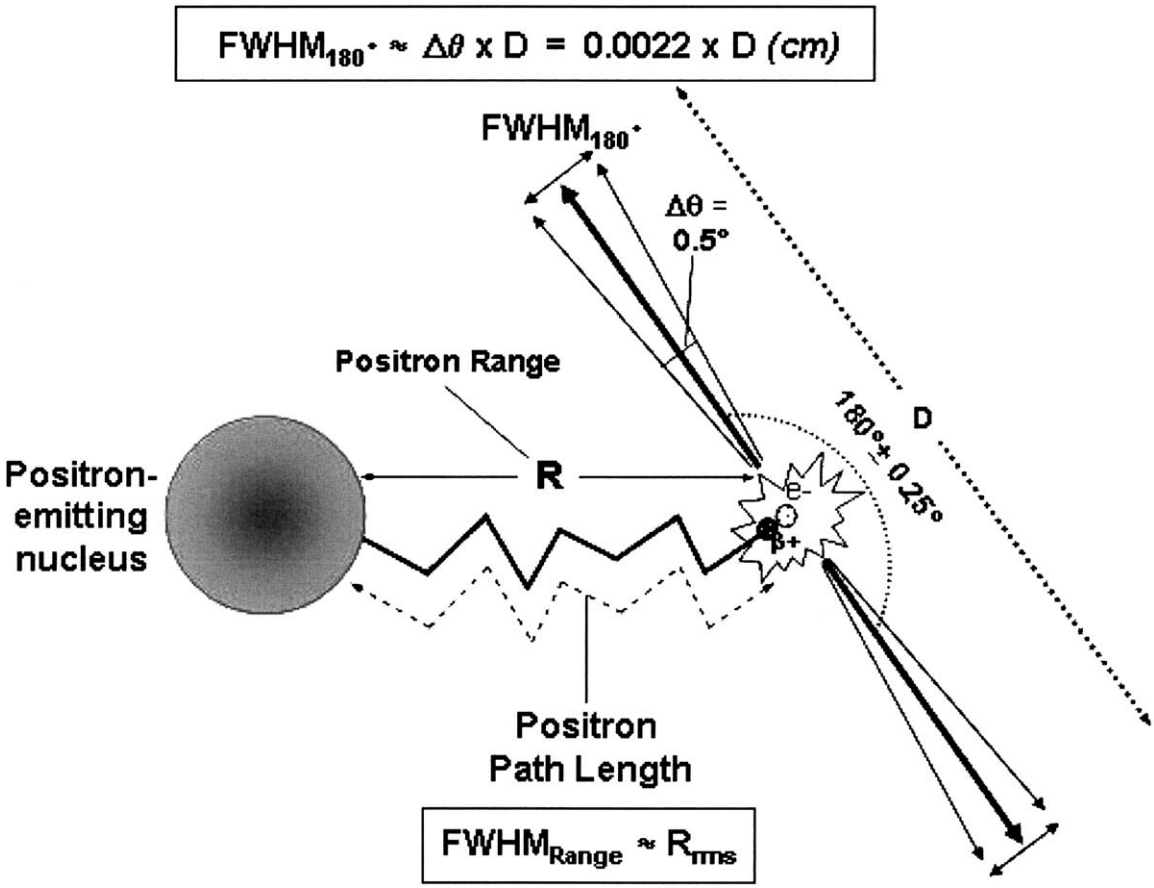

Fig 8. Physical aspects of positron-negatron annihilation and their effects on PET spatial resolution. Positrons travel a finite distance before undergoing annihilation. The range-related blurring of PET images, *FWHM*$_{Range}$, is determined by the perpendicular distance (ie, the range) rather than the total path length traveled by the positron from the decaying nucleus and is approximately equal to the root-mean-square (rms) range, R_{rms}.[24,25] In addition, the 511-keV annihilation γ-rays resulting from positron-negatron annihilation are not exactly colinear, that is, they are emitted 180 ± 0.25° apart.[26] The noncolinearity-related blurring, *FWHM*$_{180°}$, may be calculated geometrically and depends on the separation, *D*, of the coincidence detectors.[6]

and analysis protocols have been promulgated for this purpose.[21-23] The discussion below, however, addresses only several key parameters—sensitivity, spatial resolution, and noise-equivalent count rate.

Spatial Resolution

The overall spatial resolution (expressed as the full-width half-maximum [FWHM] of the line spread function) of PET scanners results from a combination of physical and instrumentation factors. There are several important limitations imposed on resolution by the basic physics of positron-negatron annihilation (Fig 8). First, for a given radionuclide, positrons are emitted over a spectrum of initial kinetic energies ranging from 0 to a characteristic maximum, or endpoint, energy, E_{max}; the associated average positron energy, $\bar{E}$, is approximately one-third of its endpoint energy, $\bar{E} \approx \frac{1}{3} E_{max}$. Positrons will therefore travel a finite distance from the decaying nucleus ranging from 0 to a maximum called the extrapolated range, R_e, corresponding to its highest-energy positrons. For positron emitters used to date in PET, the maximum energies (E_{max}) vary from 0.58 to 3.7 MeV, the extrapolated ranges (R_e) from 2 to 20 mm, and the root-mean-square (rms) ranges (R_{rms}) from 0.2 to 3.3 mm (Table 1). Although the finite positron range acts to degrade spatial resolution,[24] the range-related blurring is mitigated by the spectral distribution of positron energies for a given radio-

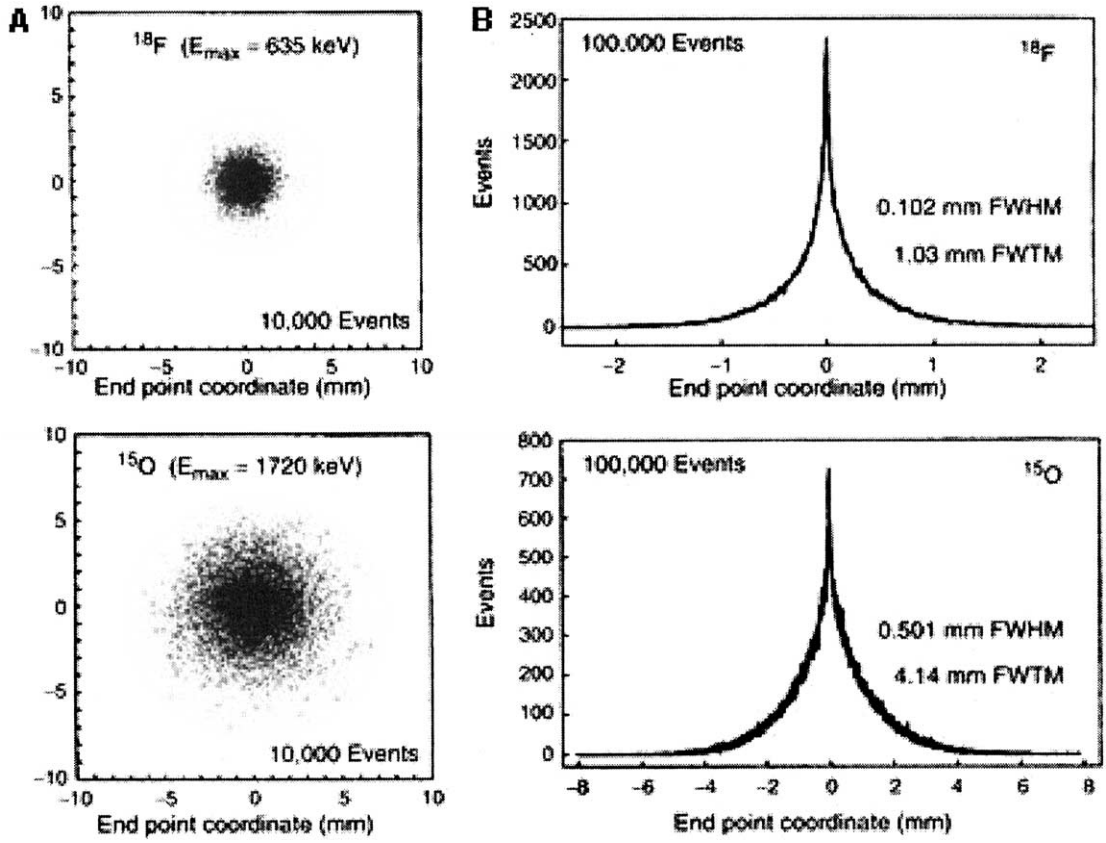

Fig 9. Effects of positron range on PET spatial resolution. (A) The spatial dispersion of positron-negatron annihilations for fluorine-18 (E_{max} = 640 keV) and oxygen-18 (E_{max} = 1720 keV) as determined by Monte Carlo simulation (10,000 histories). The annihilations for the higher-energy oxygen-18 positrons are clearly more widely dispersed than those for the lower-energy fluorine-18 positrons. (B) A graphical representation of the resulting range-related blurring in PET, $FWHM_{Range}$, as determined by Monte Carlo simulation (100,000 histories): 1.03 mm and 4.14 mm for fluorine-18 and oxygen-15, respectively. Reproduced from Levin and Hoffman[25] with permission.

isotope as well as the characteristically tortuous path positrons travel; these effects are reflected by the fact the rms positron ranges are nearly 10-fold shorter than the extrapolated positron ranges (Table 1). The perpendicular distance the positron travels is thus considerably shorter than the actual path length it travels (Fig 8). The overall effect of positron range on PET spatial resolution, $FWHM_{range}$, is illustrated quantitatively in Fig 9. The positron range degrades spatial resolution by only ~0.1 mm for fluorine-18 (E_{max} = 640 keV) and ~0.5 mm for oxygen-15 (E_{max} = 1720 keV);[25] these values are much closer to the respective rms positron ranges, 0.2 and 0.9 mm, than to the respective extrapolated positron ranges, 2.3 and 8.0 mm.

The second physics-related limitation on PET performance is the noncolinearity of the two annihilation photons: because a positron actually has some small residual (nonzero) momentum and kinetic energy at the end of its range, the two annihilation photons are not emitted exactly back-to-back (ie, 180° apart) but deviate from colinearity by up to 0.25°.[26] The noncolinearity related blurring, $FWHM_{180°}$, varies from ~2 mm for an 80-cm diameter whole-body PET to ~0.7 mm for a 30-cm diameter brain PET to ~0.3 mm for a 12-cm diameter small-animal PET (Fig 8).[6]

Among instrumentation-related determinants of overall spatial resolution are the intrinsic detector resolution and, for multi-detector ring PET scanners, the depth-of-interaction effect. For discrete, small-area detectors, resolution is determined by the detector width (w), increasing from $\frac{w}{2}$ midway between opposed coincidence detectors to w at the

face of either detector.[6] For continuous, large-area detectors with an empirically determined intrinsic resolution of $FWHM_{\text{intrinsic}}$, resolution increases from $\frac{FWHM_{\text{intrinsic}}}{\sqrt{2}}$ midway between the opposed detectors to $FWHM_{\text{intrinsic}}$ at the face of either detector.[6]

For PET systems using rings of discrete, small-area detectors, the depth of the detector elements (2-3 cm) results in a degradation of spatial resolution termed the depth-of-interaction (DOI) or parallax effect.[6] With increasing radial offset of a source from the center of a detector ring, the effective detector width and, with it, the intrinsic resolution increase[6] In whole-body PET scanners, the detector depth is typically 2 to 3 cm (20 to 30 mm), the detector width about 4 mm, and the detector ring diameter about 80 cm (800 mm) and the DOI effect thus degrades spatial resolution by 50% at 10 cm from the center of the detector ring.

Sensitivity

System sensitivity (the measured event rate per unit activity) is determined by the combination of geometric efficiency (the fraction of emitted radiations striking the detector) and intrinsic efficiency (the fraction of radiations striking a detected which are stopped in and counted by the detector). The geometric efficiency is equivalent to the fractional solid angle at the source subtended by the detector. For a ring detector of depth d and diameter D and ignoring the small interdetector area, the geometric efficiency (g) decreases linearly from approximately $\frac{d}{D}$ at the center to 0 at the end of the ring, yielding an average geometric efficiency of $\frac{d}{2D}$.[6] Based on the exponential attenuation of radiation, the single-photon intrinsic efficiency (ϵ) is given by $1\text{-}e^{-\mu d}$, where μ is the linear attenuation coefficient (in cm) of the detector material for 511-keV γ-rays and d is the thickness (in cm) of the detector. For coincidence detection of the two 511-keV annihilation γ-rays, the intrinsic efficiency is actually ϵ.[2] Because of the quadratic dependency on intrinsic sensitivity for ACD, the differential stopping power for 511-keV γ-rays is accentuated: for BGO and LSO, ϵ^2 is nearly 50% greater than for GSO and nearly three-fold greater than for NaI(Tl) (Table 2).

PET system sensitivities, for a point source at the center of the FOV, range from 0.2 to 0.5% (74-185 cps/μCi) for 2D scanners to 2 to 10% (740-1850 cps/μCi) for 3D scanners.[6] SPECT system sensitivities, on the other hand, typically have 10- and 100-fold lower sensitivities than 2D and 3D PET scanners, respectively.

Noise-Equivalent Count Rate (NECR)

The noise-equivalent count rate (NECR),[22,23] defined as follows, is a particularly important parameter of practical PET performance:

$$\text{NECR} = \frac{T^2}{T + S + R} \qquad (2)$$

where T, S, and R = the trues, scatter, and randoms count rates, respectively. The maximum NECR is thus the optimal count rate for a particular scanner. For 2D scanners, the interdetector septa effectively reduce the contribution of the scatter and randoms count rates such that the NECR is essentially equivalent to the trues rate. Thus, for 2D scanners, the NECR increases linearly with activity and there is no optimal count rate or activity (Fig 10). For 3D scanners, on the other hand, the trues and scatter count rates are proportional to the activity while the randoms count rate is proportional to the square of the activity. Thus, there exists a well-defined optimum activity for 3D scanners (Fig 10). The faster the detectors, and therefore the shorter the coincidence timing window, the lower the randoms count rate for a given activity and the higher the activity at which the maximum NECR occurs and the higher the value of the maximum NECR. A "fast" 3D LSO scanner (coincidence timing window: ~6 ns) has a maximum NECR several-fold higher than that of a "slower" 3D BGO scanner (coincidence timing window: ~12 ns) (Fig 10). A fast 3D scanner allows the use of higher administered activities and yields high "usable" count rates, short scan durations, and accelerated patient throughput. At clinical activities (eg, 185 MBq = 5 mCi to 370 MBq = 10 mCi of fluorine-18), even "slow" 3D scanners have substantially higher sensitivities and NECRs than 2D scanners.

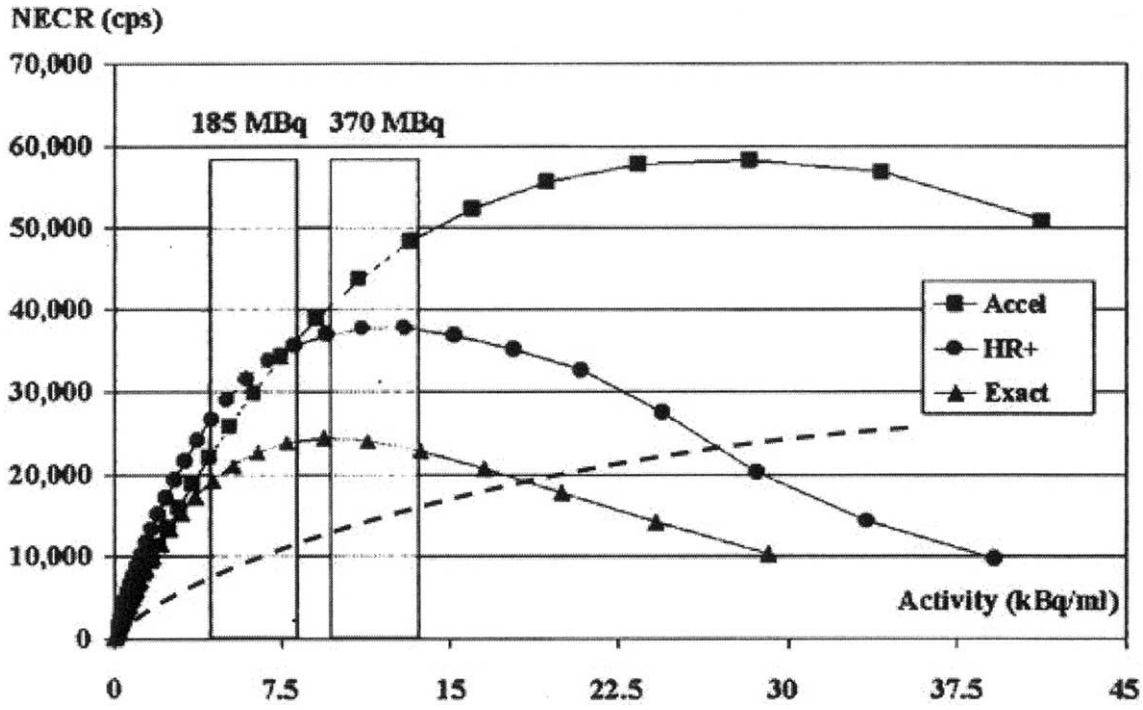

Fig 10. NECR curves, that is, noise-equivalent count rate (NECR)-versus-activity concentration curves for 2 BGO-based multi-ring PET scanners, the Siemens-CTI (Knoxville, TN) HR+ and EXACT, and an LSO-based multi-ring scanner, the Siemens-CTI Accel. A typical NECR curve (dashed line) for a 2D multi-ring PET scanner is shown for comparison. Adapted from Tarantola et al[16] with permission.

DATA PROCESSING: NORMALIZATIONS AND CORRECTIONS, IMAGE RECONSTRUCTION, AND QUANTITATION

Deadtime Correction

PET scanners have a finite deadtime and associated count losses. The deadtime is the length of time required for a counting system to fully process and record an event, during which additional events cannot be recorded. As a result, the measured count rate is systematically lower than the actual count rate. Such count losses are significant, however, only at "high" count rates (ie, greater than the inverse deadtime expressed in seconds). For multi-detector ring PET systems, deadtime count losses are generally minimal at clinical administered activities. Nonetheless, a real-time correction for deadtime count losses is routinely applied to the measured count rates. Most commonly, this is performed by scaling up the measured count rate, either per LOR or globally, based on an empirically derived mathematical relationship between measured and true count rates.

Randoms Correction

Randoms increase the detected coincidence count rate by contributing spuriously placed coincidence events and thus reduce image contrast and distort the relationship between image intensity and activity concentration. The standard approach to randoms correction, the "delayed window" method,[27] is based on the fact that the random-coincidence γ-rays are temporally uncorrelated (ie, not simultaneously emitted). Briefly, once singles in the coincidence timing window (typically 6-12 ns) are detected, the number of singles in a timing window equal in duration to, but much later ($>$50 ns later) than, the coincidence timing window are determined. The number of events in the delayed timing window provides an estimate of the number of randoms in the coincidence timing window. Real-time subtraction of the delayed-window counts from the coincidence-window counts for each LOR thus corrects for randoms.

Normalization

Even optimally performing PET scanners exhibit some nonuniformity of response. Among the

10,000 to 20,000 detector elements in a modern ring scanner, slight variations among the detector elements in thickness, light emission properties, electronics performance etc result in slightly different LOR count rates for the same activity. In principle, nonuniform response can be corrected by acquiring data for a uniform flux of annihilation γ-rays.[6,20] If LOR_T is the total number of LORs and a total of N_T events is acquired in the normalization scan, the average number of counts per LOR, $\bar{N}_{LOR}$, is simply:

$$\bar{N}_{LOR} = \frac{N_T}{LOR_T} \quad (3)$$

For the LOR between detectors i and j, LOR_{ij}, with measured number of events N_{ij}, the normalization factor NF_{ij} is:

$$NF_{ij} = \frac{\bar{N}_{LOR}}{N_{ij}} \quad (4)$$

and, for the scan of a patient, the normalized, or corrected, number of events, C'_{ij}, in this LOR is:

$$C'_{ij} = NF_{ij}C_{ij} \quad (5)$$

where C_{ij} = the raw, or uncorrected, number of events in the LOR between detectors i and j.

The normalization scan can be performed using a positron-emitting rod source (eg, germanium-68) spanning the entire axial FOV and rotating it around the periphery of the FOV, exposing the detector pairs to a uniform photon flux per revolution. Alternatively, a uniform cylinder of a positron-emitting radionuclide can be scanned and the data thus acquired analytically corrected for attenuation; for a well-defined geometry such as a uniform cylindrical source, this correction is straightforward. However, for 3D PET, the contribution of, and correction for, scatter with such a large-volume source are nontrivial. In practice, either approach is somewhat problematic because of statistical considerations. With approximately 10,000 (10^4) detector elements and 100 million ($(10^4)^2 = 10^8$) LORs in a 3D PET scanner, even at a count rate of one million (10^6) cps it would take several days to acquire the number of counts per LOR, 10,000, required to reduce the statistical uncertainty per LOR normalization factor to 1%. Alternatively, therefore, the response per detector, rather than per LOR, can be measured and the LOR normalization factors then calculated. This would require 10,000-fold fewer counts to achieve the same statistical uncertainty, 1%, as required by direct measurement of the LOR normalization factors. An optimum approach to normalization, especially for 3D PET, remains to be devised.[28]

Scatter Correction

Like randoms, scatter results in generally diffuse background counts in reconstructed PET images, reducing contrast and distorting the relationship between image intensity and activity concentration.[20] Scatter is particularly problematic in PET because of the wide energy windows (eg, 250 to 600 keV) used to maintain high sensitivity in the face of the relatively coarse energy resolution (~10% or greater) of PET detectors.[29] In 2D PET, scatter correction is rather straightforward. Once the randoms correction has been applied, the peripheral "tails" in the projection-image count profiles, presumably due exclusively to scatter, are fit to a mathematical function and then subtracted (deconvolved) from the measured profile to yield scatter-corrected profiles for tomographic image reconstruction.[6,20] Although this approach works reasonably well for 2D PET and small source volumes (eg, the brain) in 3D PET, it is not adequate for 3D PET generally.[20,30,31] Scatter corrections for 3D PET include:[20,30] dual energy window-based approaches; convolution/deconvolution-based approaches (analogous to the correction in 2D PET); direct estimation of scatter distribution (by Monte Carlo simulation of the imaging system); and iterative reconstruction-based scatter compensation approaches (also employing Monte Carlo simulation). The Monte Carlo simulation and subtraction of scatter are now practical and have been implemented in commercial PET scanners.

Attenuation Correction

Attenuation correction is the largest correction in PET. However, one of the most attractive features of PET is the relative ease of applying accurate and precise corrections for attenuation, based on the fact that attenuation depends only on the total thickness of the attenuation medium (Fig 11). For a positron-emitting source and a volume of thickness L, the attenuation factor is $e^{-\mu L}$ and the attenuation correction factor $e^{\mu L}$ regardless of

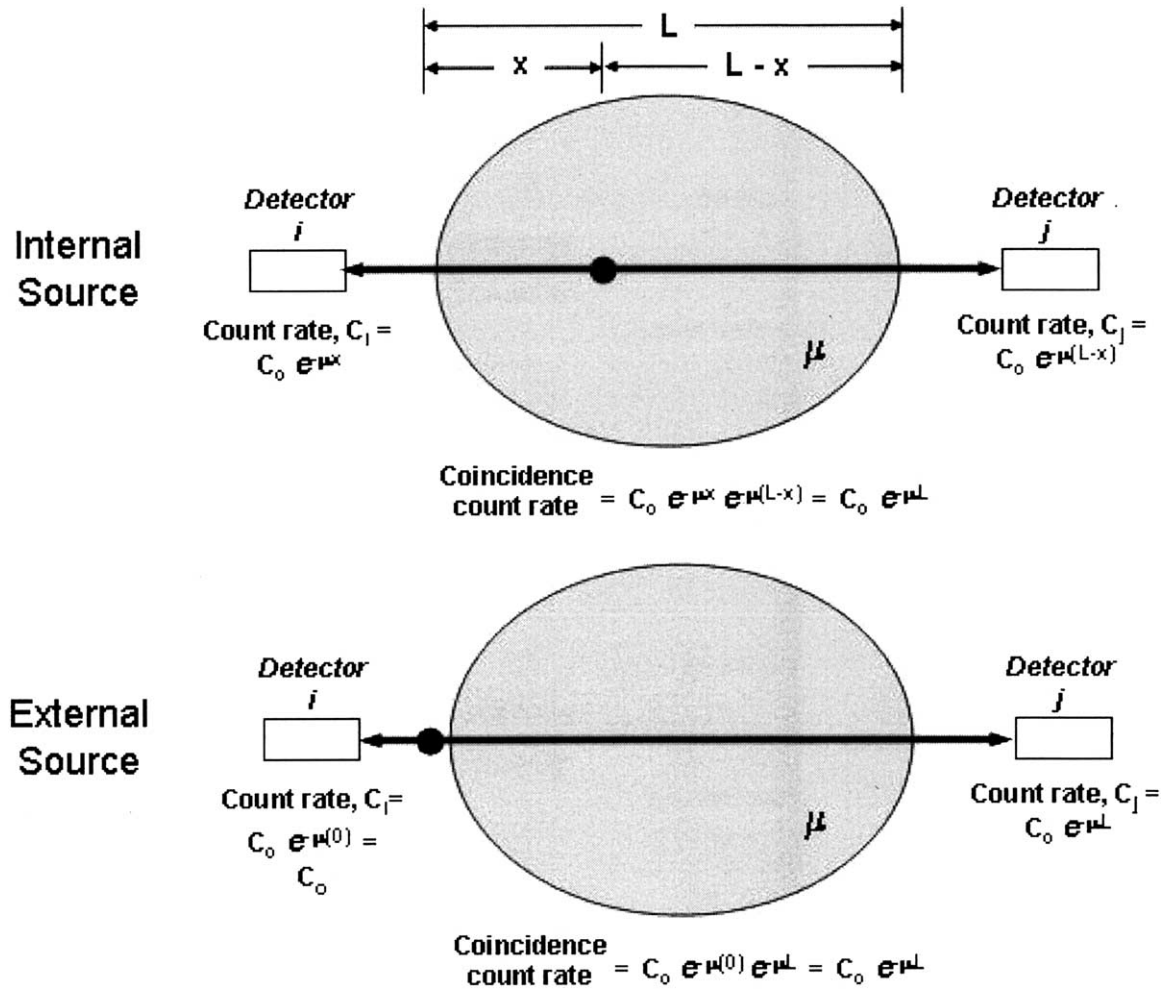

Fig 11. Attenuation of annihilation γ-rays depends only on the total thickness (L) of the absorber, that is, it is independent of the position of the source relative to the absorber.

the position of the source. Accordingly, a rod source of a positron emitter such as germanium-68 may be extended along the axial FOV and rotated around the periphery of the FOV first with and then without the patient in the imaging position to acquire the transmission and blank scans, respectively. The attenuation correction factor (ACF) can then be derived from the ratio of the counts in these respective scans:

$$ACF_{ij} = e^{\mu L_{ij}} \tag{6a}$$

$$= \frac{[(C)_{Blank}]_{ij}}{[(C)_{Trans}]_{ij}} \tag{6b}$$

where ACF_{ij} = the attenuation correction factor between coincident detectors i and j, L_{ij} = the thickness of the volume between coincident detectors i and j, and $[(C)_{Blank}]_{ij}$ and $[(C)_{Trans}]_{ij}$ = the external-source counts between detectors i and j in the blank and transmission scans, respectively. In practice, a blank scan is acquired only once a day. The transmission scan can be acquired before the patient has been injected with the radiopharmaceutical, after the patient has been injected with the radiopharmaceutical but before or after the emission scan, or after the patient has been injected with the radiopharmaceutical and at the same time as the emission scan. Preinjection transmission scanning avoids any interferences between the emission and transmission data but requires that the patient remain on the imaging table before, during, and after injection of the radiotracer. It is

the least efficient operationally and is rarely used in practice. Postinjection transmission scanning minimizes the effects of patient motion, relying on the much higher external-source count rates for reliable subtraction of the emission counts from the transmission counts. It is probably the most commonly used approach in "PET-only" scanners. Simultaneous emission/transmission scanning is obviously the most efficient (fastest) approach but may result in excessively high randoms and scatter counter rates in the emission data. The GE Advance employs postinjection transmission scanning using two germanium-68 rod sources each with 370 MBq (10 mCi) and a 4-to 6-minute transmission scan per bed position.

A notable refinement of transmission scan-based attenuation correction is the use of a single-photon emitter such as cesium-137 in place of a positron emitter.[32-35] The Philips-ADAC Allegro, for example, employs a single 370- to 740-MBq (10- to 20-mCi) cesium-137 rod source. For equal-activity sources, germanium-68 results in much lower count rates and longer transmission scan times than cesium-137 because coincidence counting of the germanium-68 results in rejection of most of its annihilation γ-rays. In addition, cesium-137 (30 years) has a much longer half-life than germanium-68 (287 days), and therefore a cesium-137 transmission source does not have to be replaced while a germanium-68 source must be replaced periodically. At the same time, the energy of the cesium-137 γ-ray, 662 keV, is significantly higher than that of the 511-keV annihilation γ-rays and, with the excellent energy resolution of GSO, there is less interference of a cesium-137 transmission scan by activity in the patient. As a result, transmission scans can be acquired more quickly since the counting statistics requirements are considerably less than for reliable subtraction of equal-energy transmission and emission counts. However, because of the difference in energies, 662 versus 511 keV, the *ACF*s derived from a cesium-137 transmission scan must be scaled slightly to adjust for the differential attenuation between 662- and 511-keV γ-rays.

Another important refinement in transmission scan-based attenuation correction is the use of segmentation.[36] In segmented attenuation correction, the regional *ACF*s are not measured. Rather, the transmission scan is used to visualize the patient's internal anatomy and then partition, or segment, it into the visualizable compartments of soft tissue, bone, and lung (air). The appropriate linear attenuation coefficients (μ)—for 511-keV γ-rays, 0.095 cm for soft tissue, 0.13 cm for bone, and 0.035 cm for lung[6]—are then applied to these respective tissue compartments and the overall *ACF*s calculated. An important advantage of this approach is that far fewer counts are required in the transmission data.[37] As a result, transmission scans for segmented attenuation correction are much faster—only 1 to 2 min—than for nonsegmented correction (4 to 6 min).

With the recent introduction of PET-CT scanners,[38-40] attenuation correction may now be performed using CT rather than transmission sources. A CT image is basically a two-dimensional map of attenuation coefficients at the CT x-ray energy (~80 keV). For attenuation correction of the PET emission data, however, these must be appropriately scaled to the 511-keV energy of the annihilation γ-rays. The mass-attenuation coefficients (μ_m) for CT x-rays (~80 keV) and for 511-keV annihilation γ-rays are 0.182 and 0.096 cm^2/gm, 0.209 and 0.093 cm^2/gm, and 0.167 and 0.087 cm^2/gm in soft tissue, bone, and lung, respectively.[41] The corresponding μ_m ratios are therefore 1.90, 2.26, and 1.92, respectively. Thus, ACFs derived from CT images cannot be scaled to those for 511-keV annihilation γ-rays simply using a global factor. Accordingly, CT-based attenuation correction in PET has been implemented using a combination of segmentation—to delineate the soft tissue, bone, and lung compartment—and variable scaling—to account for the different μ_m ratios in these respective tissues.[41] Commercial PET-CT scanners employ high-end (up to 16 slices) spiral CT scanners, and CT-based attenuation correction therefore not only provides optimal segmentation of tissue compartments but is also much faster than transmission-based corrections. However, CT-based attenuation correction is not without complications.[38,42,43] Most notably, in areas of the body with materials (such as metallic implants or foci of intravenous contrast) with radiodensities far higher than those for tissues, the attenuation may be over-corrected, resulting in the calculation of spuriously high activity concentrations. For this and other reasons, the Gemini PET-CT (Philips-ADAC) includes cesium-137 transmission line

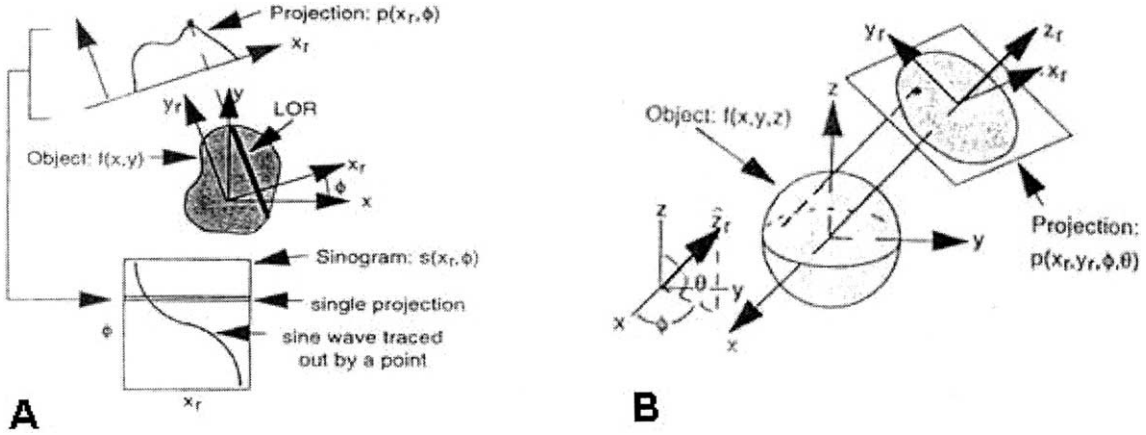

Fig 12. (A) In 2D PET, the emission data are the one-dimensional projections (sets of parallel line-integrals) of the direct planes at the azimuthal angles ϕ relative to the axis of the scanner. In the sinogram, each row represents the projected intensity across a single direct plane and each column the projected intensity at the same distance x_r across the projection at successive azimuthal angles ϕ. (B) In 3D PET, the projections are two-dimensional (x_r,y_r) parallel line-integrals with azimuthal angle ϕ and oblique angle θ. The 3D projection data are represented as a set of sinograms, with one sinogram per polar angle θ, each row representing the projected intensity across a single polar angle θ and each column the projected intensity at the same position xr across the projection at successive azimuthal angles ϕ. Reproduced from Defrise and Kinahan[44] with permission.

sources and either a CT- or a transmission scan-based attenuation correction may be applied.

Image Reconstruction

Formation of quantitative PET images requires the following data sets: an emission data file to be reconstructed; a normalization file for correction of the emission data for system response; a CT or a transmission data file for attenuation correction; and a corresponding blank (or "air") file for attenuation correction. In 2D PET, the emission data are the one-dimensional projections (sets of parallel line-integrals) of the direct planes at the azimuthal, or projection, angles ϕ relative to the axis of the scanner. The full set of 2D projection data are usually represented as a two-dimensional matrix in polar coordinates (distance x_r, angle ϕ) known as a "sinogram" (or "histogram") in which each row represents the projected intensity across a single direct plane and each column the projected intensity at the same distance x_r across the projection at successive azimuthal angles ϕ (Fig 12A).[44] In 3D PET, the projections are two-dimensional (x_r,y_r) parallel line-integrals with azimuthal angle ϕ *and* oblique, or polar, angle θ. The full set of 3D projection data are then represented as a *set* of sinograms, with one sinogram per polar angle θ. In each sinogram, each row represents the projected intensity across a single oblique plane (at polar angle θ) and each column the projected intensity at the same position across the projection at successive azimuthal angles ϕ (Fig 12B).[44]

Analytic methods for reconstruction of 3D data characteristically suffer from incomplete sampling of the 3D volume as a result of the finite axial FOV of PET scanners. The three-dimensional re-projection (3DRP) algorithm,[45,46] an extension of the standard 2D FBP algorithm (see below), has been the most widely used 3D reconstruction algorithm and has been implemented on commercial 3D scanners.[28] In 3DRP, unsampled data are estimated by reconstruction and then 3D forward-projection of an initial image set obtained by reconstruction of the directly measured data. Such 3D reconstruction algorithms remain computer-intensive and rather slow by clinical standards,[16] however. In addition, 3D PET emission data files are very large. If N_T = the total size (in bytes) of the projection data set, N_R = the number of detector rings $\approx$ 24 (typical value), N_d = the number of detector elements per ring $\approx$ 512 (typical value), and N_b = the depth of the data storage bins = 2 bytes, $N_T = N_R^2 \frac{Nd}{2} N_b$ = 0.3 MByte for 2D PET and $N_T = N_R^2 \left(\frac{Nd}{2}\right)^2 N_b$ = 75 Mbytes for 3D PET.[44] Thus, 3D data sets are more than two orders of magnitude larger than 2D data sets. It is prefer-

able, therefore, to reduce 3D data sets to a more manageable size for image reconstruction—by re-binning of the 3D set of oblique sinograms into a smaller number of direct 2D sinograms. The simplest method is "single-slice re-binning (SSRB)," wherein true oblique LORs are assigned to the direct plane midway between the two detector elements actually in coincidence.[47] Although still used on Anger camera-based systems,[16] SSRB distorts off-axis activity and thus is accurate only for activity distributions close to the detector axis,[44] as in brain or small-animal imaging. A second method is multi-slice re-binning (MSRB),[48] which is fast but is susceptible to "noise"-related artifacts.[44] The current method of choice is Fourier re-binning (FORE),[49] based on the 2D Fourier transform of the oblique sinograms. In contrast to SSRB and MSRB, however, FORE cannot be performed in real-time and thus requires the full 3D data set.

After 2D re-binning of 3D data, 2D reconstruction algorithms can used for 3D as well as 2D PET data. Note that processing of the emission data after the real-time deadtime and random corrections and before image reconstruction—namely, normalization, scatter correction, and then attenuation correction—is normally performed in sinogram space.

One of the most widely used algorithms for reconstruction of tomographic images from 2D data (or 3D data re-binned into 2D projections)—in SPECT as well as PET—remains filtered back-projection (FBP).[50] The basic procedure is as follows: each projection is Fourier transformed from real to frequency space; the projection is filtered in frequency space using a ramp filter; the filtered projection is inverse Fourier transformed from frequency back to real space; and the filtered projection data in real space are uniformly distributed, or back-projected, over the reconstructed image matrix.[16,44,50] The resulting reconstructed image is inexact, however, because the ramp filter results in the inclusion of spatial frequencies beyond the maximum frequency image-able by the scanner (ie, the Nyquist frequency, ν_N)—producing aliasing artifacts (such as the "starburst" pattern emanating from discrete, high-activity foci)—and amplifies statistical uncertainty (noise or mottle).[16,44] To compensate for these effects, low-pass, or apodizing, filters (known as Hanning, Butterworth, etc.) are used in place of the ramp filter to eliminate those spatial frequencies above a cut-off frequency, ν_c, set equal to ν_N or some fraction thereof. Although the resulting reconstructed images have somewhat degraded spatial resolution, they are far less "noisy" (mottled).

In contrast to so-called "transform" reconstruction methods such as FBP, iterative algorithms attempt to progressively refine estimates of the activity distribution, rather than directly calculate the distribution, by maximizing or minimizing some "target function." The solution is said to "converge" when the difference of the target function between successive estimates (iterations) of the activity distribution is less than some prespecified value. Importantly, iterative reconstruction algorithms allow incorporation of realistic modeling of the data acquisition process (including effects of attenuation and of scatter), modeling of statistical noise, and inclusion of pertinent a priori information (eg, only nonnegative count values). The maximum-likelihood expectation maximization (MLEM) algorithm is based on maximizing the logarithm of a Poisson-likelihood target function.[51,52] The MLEM algorithm suppresses statistical noise, but large numbers of iterations typically are required for convergence and therefore processing times are long. To accelerate this slow convergence, the ordered-subset expectation maximization (OSEM) algorithm[53] groups the projection data into subsets comprised of projections uniformly distributed around the source volume. The OSEM algorithm, which is a modified version of the MLEM algorithm in that the target is still maximization of the log-likelihood function, converges more rapidly than MLEM and is now the most widely used iterative reconstruction method in PET as well as SPECT.[16] The row-action maximization-likelihood (RAMLA) algorithm, related to the OSEM algorithm, has been implemented for direct reconstruction of 3D PET data in the C-PET and Allegro (Philips ADAC). The so-called 3D-RAMLA algorithm, which eliminates 2D re-binning of the 3D data, employs partially overlapping, spherically symmetric volume elements called "blobs" in place of voxels.[16,54,55] Reconstruction times are fairly long by clinical standards but the results have been excellent.[56]

Quantitation

Once the PET emission data have been corrected for deadtime, randoms, system response (by nor-

malization), scatter, and attenuation, the count rate per voxel in the reconstructed tomographic images is proportional to the local activity concentration. To make the images quantitative, then, the count rate per voxel (cps), C_{ijk}, in voxel ijk should be divided by the measured system calibration factor ([cps/voxel]/[μCi/cc]), CF, to yield the activity concentration:

$$[A]_{ijk} = \frac{\dot{C}_{ijk}}{CF} \quad (7)$$

where $[A]_{ijk}$ = the activity concentration (μCi/cc) in voxel ijk. The calibration factor CF can be derived by scanning a calibrated standard, that is, a water-filled or water (tissue)-equivalent volume source with all linear dimensions at least twice that of the system spatial resolution (FWHM) and with a uniform, well-defined activity concentration at the time of the scan. The requirement for water equivalence is to ensure that effects such as scatter and attenuation are comparable in both the patient and the standard. And the requirement for linear dimensions at least twice that of the system spatial resolution is to ensure that the effect of partial volume averaging and associated underestimation of local count rates are negligible. (Unless corrected for partial-volume averaging based on some independent measure of size, activity concentrations cannot be reliably determined in structures with dimensions less than twice the system spatial resolution.[57]) In principle, assuming the emission data for the patient and the standard are processed identically, the geometry of the standard should be unimportant. In practice, a fairly large source such as cylinder spanning the scanner's axial FOV and approaching the transverse dimensions of typical patients is preferable. Further, implicit in equation (7) is the assumption that the branching ratios, ζ, of the positron-emitter administered to the patient and added to the standard are identical. If not, equation (10) must be appropriately adjusted:

$$[A]_{ijk} = \frac{\dot{C}_{ijk}}{CF} \frac{\zeta_{Standard}}{\zeta_{Patient}} \quad (8)$$

where $\zeta_{Patient}$ and $\zeta_{Standard}$ = the branching ratio of the positron-emitting isotope administered to the patient and added to the standard, respectively.

Typically, a more clinically relevant expression of local activity concentration is in terms of the decay-corrected fraction or percent of the administered activity per cubic centimeter (cc). This requires, however, that one precisely assay and record the actual activity in the radiopharmaceutical syringe before and after the injection and record the precise times of the assays and of the scan. The percent of the injected activity per cubic centimeter of tissue, % ID/cc, can then be calculated as follows:

$$\%ID/cc = \frac{\frac{\dot{C}_{ijk}}{CF} \frac{\zeta_{Standard}}{\zeta_{Patient}} e^{\lambda (t_{scan} - t_{inj})}}{(A_{syringe})_{Pre} - (A_{syringe})_{Post}} \times 100\% \quad (9)$$

where t_{scan} and t_{scan} = the times of the PET scan and of the radiopharmaceutical injection, respectively, and $(A_{syringe})_{Pre}$ and $(A_{syringe})_{Post}$ = the net activities (decay-corrected to the time of injection) in the radiopharmaceutical syringe before and after the injection, respectively. Clinically, however, the most widely used expression of the activity concentration is the standard uptake value (SUV), the ratio of the activity concentration in tumor or other tissue at the time of the PET scan to that of the mean activity concentration in the total body at the time of injection:

$$SUV \equiv \frac{\mu Ci/mL \text{ of tissue}}{\mu Ci \text{ injected/g body mass}} \quad (10a)$$

$$= \frac{\frac{\dot{C}_{ijk}}{CF} \frac{\zeta_{Standard}}{\zeta_{Patient}} e^{\lambda (t_{scan} - t_{inj})}}{\frac{(A_{syringe})_{Pre} - (A_{syringe})_{Post}}{M_{Patient}}} \quad (10b)$$

where $M_{patient}$ = the total-body mass (in gm) of the patient.

CURRENT PET SYSTEMS

Clinical Systems

Today, turn-key PET systems, with such advanced features as detector elements numbering in the thousands, septa-less three-dimensional data acquisition, and iterative image reconstruction and yielding quantitative whole-body images with a spatial resolution of ~5 mm in less than 20 to 30 minutes, are marketed by a number of major manufacturers, including General Electric, Siemens-CTI, and Philips-ADAC. Multiple full rings of BGO, GSO, or LSO block or pixelated detectors are the prevailing design among the highest-performing devices. Systems comprised of rotating

partial rings of such detectors are also available as are systems comprised of polygons of flat or curved large-area detectors. A detailed tabulation of the design and performance parameters of the major dedicated PET scanners currently available is presented in Tables 3 and 4.

The major manufacturers of PET scanners now also market multi-modality scanners,[39,40] combining high-performance state-of-the-art PET and CT scanners in a single device. These instruments provide near-perfect registration of images of in vivo function (PET) and anatomy (CT) and are already having a major impact on clinical practice, particularly in oncology.[58] PET–CT devices are currently outselling "PET-only" systems by a two-to-one ratio.[59] Although generally encased in a single seamless housing, the PET and CT gantries in such multi-modality devices are separate; the respective FOVs are separated by a distance of the order of 1 m and the PET and CT scans are performed sequentially. In one such device, the Gemini (Philips-ADAC), the PET and CT gantries are actually in separate housings with a sizable space between them; this not only provides access to patients but also may minimize anxiety among claustrophobic subjects. Moreover, in the Gemini the distance between the PET and CT gantries may be varied. A tabulation of the design parameters of the CT scanners in PET-CT devices currently available is presented in Table 5.

The spiral CT scanners incorporated into PET-CT devices are extremely fast, potentially allowing the completion of a whole-body scan in a matter of seconds or even a single breadth hold. In contrast, PET scanners are much slower, requiring at least several minutes and a number of respiratory cycles per bed position. The use of single-breadth CT data for attenuation correction of such ungated, multi-breadth PET data has been shown to introduce artifacts—both qualitative and quantitative—in the PET images.[38,42,43] Nehmeh and coworkers[42,43] have developed and applied methods for gated PET acquisition and have demonstrated that the foregoing artifacts can be effectively eliminated by such an approach.

The clinical application of PET in general and PET-CT in particular is growing rapidly,[58,60] especially in oncology. With the incorporation of 16-slice spiral CT scanners,[59] applications in cardiology are likely to grow as well. At the same time, the integration of PET and CT image data will likely become more seamless. With the advent of intensity-modulated radiation therapy (IMRT), a major clinical application of PET-CT will no doubt be functional imaging-based treatment planning for radiation oncology.[61] PET-CT "simulators" will require appropriate modification of PET-CT scanners,[7,38] including larger patient ports (at least 70-cm-diameter continuous bore) to accommodate the patient and any immobilization cast, position indexing of image planes to an external marker (eg, laser) system for correlation with the coordinate system of the therapy unit, and respiratory gating.[42,43]

Laboratory Systems

With the development of transgenic and knockout rodent models of human disease, noninvasive imaging of small laboratory animals (ie, rats and mice) has emerged as a key component of the burgeoning field of molecular imaging.[62-68] The small sizes of such animals, and of their organs and tumors ($\sim\frac{1}{100}$ and $\sim\frac{1}{1000}$ in rats and mice, respectively, of the corresponding sizes in humans), imposes requirements for spatial resolution that are largely unattainable with even the highest-performing clinical PET scanners. To address the growing demand for ultra-high-resolution PET imaging of rodents, at least four manufacturers are currently marketing dedicated laboratory systems: the microPET (Concorde Microsystems, Knoxville, TN), with the "R4" designed for rodents and the "P4" and newer "Focus" designed for primates;[69-71] the YAP-(S)PET (ISE, Migliarino Pisano, Italy),[7,72] with both positron and single-photon imaging capabilities; the HIDAC PET (Oxford Positron Systems Ltd, Oxfordshire, UK);[65,73,74] and the Mosaic (Philips-ADAC).

The microPET is a 3D PET scanner employing 8×8-array, $2.1\times2.1\times10$ mm^3 LSO block detectors coupled to position-sensitive PMTs (PS-PMTs) via bundled 1-mm^2 optical fibers. A rotating and translating germanium-68 source can be used for acquiring a normalization file and for attenuation correction. Its spatial resolution is $\sim$2 mm, volume resolution $\sim$8 mm^3, and sensitivity 900 cps/μCi. The axial and radial FOVs, respectively, are 7.9 and 10 cm for the R4, 7.9 and 19 cm for the P4, and 7.7 and 19 cm for the Focus. The Focus achieves improved resolution, of $\sim$1 mm, by increasing the detector packing fraction.

Table 3. Design and Performance Parameters of Current Commercial PET Scanners*†

	Siemens-CTI ECAT Exact	SiemensCTI ECAT HR+	Siemens-CTI Accel	GE Advance	GE Discovery LS PET/CT	GE Discovery ST PET/CT	Philips-ADAC C-PET	CPS BGO PET/CT	CPS LSO PET/CT	Philips-ADAC Allegro/Gemini PET/CT
Patient port diameter	56.2 cm	56.2 cm	56.2 cm	58 cm	59 cm	70 cm	62 cm	70 cm	70 cm	56.5 cm
Scintillation crystal	BGO	BGO	LSO	BGO	BGO	BGO	curved NaI(Tl)	BGO	LSO	GSO
Total # of blocks	144	288	144	168	168	280	N/A	288	144	28
No. of crystal detectors/block	8 × 8	8 × 8	8 × 8	6 × 6	6 × 6	6 × 6	N/A	8 × 8	8 × 8	22 × 29
Crystal dimensions										
Transaxial	6.39 mm	4.39 mm	6.45 mm	4.0 mm	4.0 mm	6.2 mm	47 cm circum	4.39 mm	6.45 mm	4 mm
Axial	6.39 mm	4.05 mm	6.45 mm	8.0 mm	8.0 mm	6.2 mm	30 cm	4.05 mm	6.45 mm	6 mm
Radial	20 mm	30.0 mm	25 mm	30.0 mm	30.0 mm	30.0 mm	2.54 cm	30.0 mm	25 mm	20 mm
No. of detector rings	24	32	24	18	18	24	N/A	32	24	
Detector ring diameter	82.4 cm	82.4 cm	92.7 cm	92.7 cm	92.7 cm	88.0 cm	62.0 cm	82.4 cm	82.4 cm	90 cm
Total # of detectors	9,216	18,432	9,216	12,096	12,096	10,080	6 curved NaI:Tl	18,432	9,216	17,864
Transaxial field of view	58.5 cm	58.5 cm	58.5 cm	50 cm	55 cm	60 cm	57.6 cm	58.5 cm	58.5 cm	57.6 cm
Axial field of view	16.2 cm	15.5 cm	16.2 cm	15.2 cm	15.2 cm	15.2 cm	25.6 cm	15.5 cm	16.2 cm	18 cm
Slice thickness	3.37 mm	2.46 mm	3.375 mm	4.25 mm	4.25 mm	3.23 mm	4.0 mm (body)	2.43 mm	3.4 mm	2 mm
No. of slices	47	63	47	35	35	47	64	63	47	90
Coincidence timing window τ	12 ns	12 ns	6 ns	12 ns	12.5 ns	11.7 ns	8 ns	12 ns	6 ns	8 ns
Coincidence timing resolution	6 ns	6 ns	3 ns	6 ns	6 ns	6 ns		6 ns	3 ns	4 ns
Energy window	350-650 keV	350-650 keV	350-650 keV	300-650 keV	300-650 keV	300-650 keV	435-665 keV	350-650 keV	350-650 keV	
Sensitivity 2D trues NEMA 94 phantom	180 kcps/μCi/cc	200 kcps/μCi/cc	200 kcps/μCi/cc	217 kcps/μCi/cc	146 kcps/μCi/cc	300 kcps/μCi/cc	N/A	N/A	N/A	N/A
Sensitivity 2D trues+scatter NEMA 94 phantom	214 kcps/μCi/cc	244 kcps/μCi/cc	238 kcps/μCi/cc	238 kcps/μCi/cc	159 kcps/μCi/cc	348 kcps/μCi/cc	N/A	N/A	N/A	N/A
Sensitivity 3D trues NEMA 94 phantom	780 kcps/μCi/cc	900 kcps/μCi/cc	925 kcps/μCi/cc	1,261 kcps/μCi/cc	838 kcps/μCi/cc	1,280 kcps/μCi/cc	444 kcps/μCi/cc	1,049 kcps/μCi/cc	999 kcps/μCi/cc	>700 kcps/μCi/cc
Sensitivity 3 D trues+scatter NEMA 94 phantom	1,218 kcps/μCi/cc	1,406 kcps/μCi/cc	1,445 kcps/μCi/cc	1,941 kcps/μCi/cc	1,297 kcps/μCi/cc	1,800 kcps/μCi/cc	592 kcps/μCi/cc	1,586 kcps/μCi/cc	1,514 kcps/μCi/cc	>1,000 kcps/uCi/cc
2D Axial Resolution							N/A	N/A	N/A	N/A
FWHM at 0 cm	4.5 mm	4.2 mm	4.3 mm	4.2 mm	4.0 mm	5.0 mm				
FWHM at 10 cm	5.9 mm	5.0 mm	6.0 mm	5.5 mm	5.4 mm	6.5 mm				
FWHM at 20 cm	N/A	6.8 mm	N/A	7.4 mm	6.6 mm	N/A				
3D Axial Resolution										
FWHM at 0 cm	4.6 mm	3.5 mm	4.7 mm	6.0 mm	6.0 mm	5.0 mm	6.2 mm	4.2 mm	5.8 mm	4.2 mm
FWHM at 10 cm	6.5 mm	5.3 mm	7.1 mm	6.3 mm	6.3 mm	6.5 mm	6.9 mm	5.7 mm	7.1 mm	5.6 mm
FWHM at 20 cm	N/A	7.8 mm	N/A	6.6 mm	6.6 mm	N/A	8.0 mm	N/A	N/A	N/A
2D Transaxial Resolution							N/A	N/A	N/A	N/A
FWHM at 1 cm	6.0 mm	4.6 mm	6.2 mm	5.1 mm	4.8 mm	6.2 mm				
FWHM at 10 cm	6.7 mm	5.4 mm	6.7 mm	5.7 mm	5.4 mm	7.0 mm				
FWHM at 20 cm	N/A	7.9 mm	N/A	7.2 mm	6.2 mm	7.5 mm				
3D Transaxial Resolution										
FWHM at 1 cm	6.0 mm	4.6 mm	6.3 mm	5.1 mm	4.8 mm	6.2 mm	5.7 mm	4.5 mm	6.3 mm	4.8 mm
FWHM at 10 cm	6.7 mm	5.4 mm	6.8 mm	6.0 mm	5.4 mm	7.0 mm	5.7 mm	5.6 mm	7.4 mm	5.9 mm
FWHM at 20 cm	N/A	7.8 mm	N/A	7.4 mm	6.2 mm	7.5 mm	N/A	N/A	N/A	N/A
Scatter fraction 2D	16%	18%	16%	9%	9%	16%	N/A	N/A	N/A	N/A
Scatter fraction 3D *NEMA 1994	36%	36%	36%	36%	36%	29%	25%	37%	34%	< 30%
Randoms = Trues count rate	345 kcps	570 kcps	850 kcps (3D)	486 kcps (HS) 330 kcps (HR)	460 kcps (HS)		Never achieved Due to dead-time	679 kcps (3D)		119 @0.27mCi
50% dead-time count rate	345 kcps	635 kcps	850 kcps (3D)	474 kcps (HS) 289 kcps (HR)	505 kcps (HS) 304 kcps (HR)		38 @0.11mCi	356 kcps (3D)	434 kcps (3D)	116 @0.24mCi
Peak noise equivalent count rate	25 kcps	38 kcps	60 kcps	40 kcps	40 kcps	62 kcps	49 kcps	38 kcps	44 kcps	48 kcps

*Adapted with permission.[7]

†The reader is referred to the references 22 and 23 for further explanation of the performance parameters.

Table 4. Operational Features of Current Commercial PET Scanners*

Feature	Siemens-CTI ECAT Exact	Siemens-CTI ECAT HR+	Siemens-CTI Accel	GE ADVANCE/ADVANCE Nxi	Philips-ADAC C-PET	Philips-ADAC Allegro
Filtered backprojection	Yes (2D/3D)	Yes (2D/3D)	Yes (2D/3D)	Yes (2D/3D)	Yes (3D)	Yes (3D)
Iterative algorithms	OSEM (2D) FORE/OSEM	OSEM (2D) FORE/OSEM	OSEM (2D) FORE/OSEM	OSEM (2D)	FORE/OSEM 3D-RAMLA	FORE/OSEM 3D-RAMLA
Transmission source (Non-PET-CT scanner)	^{68}Ge	^{68}Ge	^{68}Ge	^{68}Ge	^{137}Cs	^{137}Cs also included with Gemini PET-CT
Source activity (MBq)	120 (×3)	140 (×3)	185 (×3)	370 (×2) 56 MBq (×1) for calibration	185 (×1)	740 (×1)
Source geometry	Rod	Rod	Rod	Rod	Point	Point
Transmission energy window	350-650	350-650	350-650	300-650	595-860	600-720
Whole-body scan length	195	195	195	170	168	198

*Adapted with permission.[16]

The YAP-(S)PET[7,72] is comprised of a rotating rectangular assembly of four detector modules, each comprised of a 20×20 mm^2 $YAlO_3$:Ce (cerium-activated yttrium aluminum perovskite) crystal coupled to a 3-inch PS-PMT. The opposed detectors, which operate in 3D mode, can move radially to achieve separation distances of 10 to 25 cm. The sensitivity at the center of the FOV is 640 cps/μCi (15-cm detector separation), the spatial resolution 1.8 mm, and the volume resolution 5.8 mm^3. The YAP-(S)PET has axial and radial FOVs of 4 cm.

The HIDAC-PET scanner[65,73,74] utilizes high-density avalanche gas chamber (HIDAC) detectors. The latest version of this scanner, the Quad-HIDAC, employs four detectors, each comprised of eight multi-wire proportional gas chambers with

Table 5. Technical Parameters of CT Scanners in Current Commercial PET-CT Scanners*

	PhilipsADAC Gemini	Siemens-CTI Reveal/CPS Biograph	GE Discovery LS
PET scanner	Allegro	ECAT HR+ or Accel	Advance Nxi
CT scanner	MX 8000 Dual	SomAtom Emotion Duo	Lightspeed Plus
Maximum power (kW)	60	40	60
Maximum tube voltage (kV)	140	130	140
Maximum tube current (mA)	500	240	440
Selectable kV values	90, 120, 140	80, 100, 130	80, 100, 120, 140
mA range	30-500	30-240	10-440
Heat capacity (MHU)	6.5	3.5	6.3
Slices/rotation	2	2	4
Slice number × thickness (mm)			2 × 0.625 (axial only)
2 × 0.5		2 × 1	1 and 4 × 1.25
2 × 1		2 × 1.5	4 × 2.5
2 × 2.5		2 × 2.5	4 × 3.75
2 × 5		2 × 4	4 × 5
2 × 8		2 × 5	2 × 7.5
2 × 10			2 × 10
Pitch minimum	0.375	0.25	0.75
Pitch maximum	2	2	1.5
Angular speed (s/rotation)	0.5, 0.75, 1, 1.5, 2	0.8, 1, 1.5	0.5, 0.6, 0.7, 0.8, 0.9, 1, 2, 3, 4
Maximum scan time (s)	60	100	120
Detectors array	672 × 2 (1,344 elements)	672 × 2 (1,344 elements)	912 × 16 (14,592 elements)
Transverse FOV (mm)	500	500	500

*Adapted with permission.[16]

increasing dimensions toward the edges of the detector. The sensitivity is 670 cps/μCi, the spatial resolution ~1 mm, and the volume resolution ~1 mm^3. The Quad-HIDAC has axial and radial FOVs of 28 and 17 cm, respectively.

The Mosaic is a 3D scanner employing GSO-based pixelated detectors and a rotating and translating cesium-137 source for attenuation correction. Its spatial resolution is ~2 mm. The axial and radial FOVs are 11.5 and 15 cm, respectively.

REFERENCES

1. Nutt R: The history of positron emission tomography. Mol Imaging Biol 4:11-26, 2002
2. Phelps ME, Cherry SR: The changing design of positron imaging systems. Clin Positron Imaging 1:31-45, 1998
3. Conti PS, Lilien DL, Hawley K, et al: PET and [18F]-FDG in oncology: a clinical update. Nucl Med Biol 23:717-735, 1996
4. Hoh CK, Schiepers C, Seltzer MA, et al: PET in oncology: Will it replace the other modalities? Semin Nucl Med 27:94-106, 1997
5. Gambhir SS, Czernin J, Schwimmer J, et al: A tabulated summary of the FDG PET literature. J Nucl Med 42:1S-93S, 2001
6. Cherry SR, Sorenson JA, Phelps ME: Physics in Nuclear Medicine (3rd ed). Philadelphia, PA, Saunders, 2003, pp 325-359
7. Humm JL, Rozenfeld A, Del Guerra A: From PET detectors to PET scanners. Eur J Nucl Med Mol Imaging 30:1574-1594, 2003
8. Weber D, Eckerman K, Dillman L, et al: MIRD: Radionuclide Data and Decay Schemes. New York, Society of Nuclear Medicine, 1989, 447 pp
9. Firestone RB, Shirley VS (eds). Table of Isotopes, 8th ed. New York, John Wiley & Sons, 1996
10. Graham MC, Pentlow KS, Mawlawi O, et al: An investigation of the physical characteristics of 66Ga as an isotope for PET imaging and quantification. Med Phys 24:317-326, 1997
11. Pentlow KS, Finn RD, Larson SL, et al: Quantitative imaging of yttrium-86 with PET: the occurrence and correction of anomalous apparent activity in high density regions. Clin Positron Imaging 3:85-90, 2000
12. Nutt R: For: Is LSO the future of PET? Eur J Nucl Med Mol Imaging 29:1523-1525, 2002
13. Karp JS: Against: Is LSO the future of PET? Eur J Nucl Med Mol Imaging 29:1525-1528, 2002
14. Melcher CL, Schweitzer JS: Cerium-doped lutetium oxyorthosilicate: a fast, efficient, new scintillator. IEEE Trans Nucl Sci. NS- 39:502-505, 1992
15. Kadrmas DJ, Christian PE: Comparative evaluation of lesion detectability for 6 PET imaging platforms using a highly reproducible whole-body phantom with (22)Na lesions and localization ROC analysis. J Nucl Med 43:1545-1554, 2002
16. Tarantola G, Zito F, Gerundini P: PET instrumentation and reconstruction algorithms in whole-body applications. J Nucl Med 44:756-769, 2003
17. Casey ME, Nutt R: A multi-slice two-dimensional BGO detector system for PET. IEE Trans Nucl Sci NS- 33:760-763, 1986
18. Muehllehner G, Karp JS, Surti S: Design considerations for PET scanners. Q J Nucl Med 46:16-23, 2002
19. Bendriem B, Townsend DW (eds): The Theory and Practice of 3D PET. Dordrecht, The Netherlands, Kluwer Academic Publishers, 1998
20. Bailey D, Gilardi MC, Grootoonk S, et al: Quantitative procedures in 3D PET, in Bendriem B, Townsend DW (eds): The Theory and Practice of 3D PET. Dordrecht, The Netherlands, Kluwer Academic Publishers, 1998, pp 55-109
21. Daube-Witherspoon ME, Karp JS, Casey ME, et al: PET performance measurements using the NEMA NU 2-2001 standard. J Nucl Med 43:1398-409, 2002
22. NEMA Standards Publication NU2–1994: Performance Measurement of Positron Emission Tomographs. Washington, DC, National Electrical Manufacturers Association (NEMA), 1994
23. NEMA Standards Publication NU2–2001: Performance Measurement of Positron Emission Tomographs. Washington, DC, National Electrical Manufacturers Association (NEMA), 2001
24. Derenzo SE: Mathematical removal of positron range blurring in high-resolution tomography. IEEE Trans Nucl Sci NS- 33:565-569, 1986
25. Levin CS, Hoffman EJ: Calculation of positron range and its effect on the fundamental limit of positron emission tomography system spatial resolution. Phys Med Biol 44:781-799, 1999
26. Berko S, Hereford FL: Experimental studies of positron interactions in solids and liquids. Rev Modern Phys 28:299-307, 1956
27. Hoffman EJ, Huang SC, Phelps ME, et al: Quantitation in positron emission computed tomography: 4. Effect of accidental coincidences. J Comput Assist Tomogr 5:391-400, 1981
28. Townsend DW, Bendriem B: Introduction to 3D PET, in Bendriem B, Townsend DW (eds): The Theory and Practice of 3D PET. Dordrecht, The Netherlands, Kluwer Academic Publishers, 1998, pp 1-10
29. Thompson CJ: The problem of scatter correction in positron volume imaging. IEEE Trans Med Imaging 12:124-132, 1993
30. Zaidi H: Comparative evaluation of scatter correction techniques in 3D positron emission tomography. Eur J Nucl Med 27:1813-1826, 2000
31. Zaidi H: Scatter modelling and correction strategies in fully 3-D PET. Nucl Med Commun 22:1181-1184, 2001
32. Jones W, Vaigneur K, Young J, et al: The architectural impact of single photon transmission measurements on full-ring 3D positron tomography. IEEE Nucl Sci Symp Med Imaging Conf Rec 2:1026-1030, 1995
33. Jones WF, Digby WM, Luk WK: Optimizing rod window width in positron emission tomography. IEEE Trans Med Imaging 14:266-270, 1995
34. Watson CC, Jones WF, Brun T, et al: Design and performance of a single photon transmission measurement for

the ECAT ART. IEEE Nucl Sci Symp Med Imaging Conf Rec 2:1366-1370, 1997

35. Meikle SR, Bailey DL, Hooper PK, et al: Simultaneous emission and transmission measurements for attenuation correction in whole-body PET. J Nucl Med 36:1680-1688, 1995

36. Xu EZ, Mullani NA, Gould KL, et al: A segmented attenuation correction for PET. J Nucl Med 32:161-165, 1991

37. Meikle SR, Dahlbom M, Cherry SR: Attenuation correction using count-limited transmission data in positron emission tomography. J Nucl Med 34:143-150, 1993

38. Schoder H, Erdi YE, Larson SM, et al: PET/CT: a new imaging technology in nuclear medicine. Eur J Nucl Med Mol Imaging 30:1419-1437, 2003

39. Beyer T, Townsend DW, Blodgett TM: Dual-modality PET/CT tomography for clinical oncology. Q J Nucl Med 46:24-34, 2002

40. Beyer T, Townsend DW, Brun T, et al: A combined PET/CT scanner for clinical oncology. J Nucl Med 41:1369-1379, 2000

41. Kinahan PE, Townsend DW, Beyer T, et al: Attenuation correction for a combined 3D PET/CT scanner. Med Phys 25:2046-2053, 1998

42. Nehmeh SA, Erdi YE, Ling CC, et al: Effect of respiratory gating on quantifying PET images of lung cancer. J Nucl Med 43:876-881, 2002

43. Nehmeh SA, Erdi YE, Ling CC, et al: Effect of respiratory gating on reducing lung motion artifacts in PET imaging of lung cancer. Med Phys 29:366-371, 2002

44. Defrise M, Kinahan P: Data acquisition and image reconstruction for 3D PET, in Bendriem B, Townsend DW (eds): The Theory and Practice of 3D PET. Dordrecht, The Netherlands, Kluwer Academic Publishers, 1998, pp 11-53

45. Colsher JG: Fully three-dimensional positron emission tomography. Phys Med Biol 20:103-115, 1980

46. Kinahan P, Rogers JG: Analytic three-dimensional image reconstruction using all detected events. IEEE Trans Nucl Sci NS- 36:964-968, 1989

47. Daube-Witherspoon ME, Muehllehner G: Treatment of axial data in three-dimensional PET. J Nucl Med 28:1717-1724, 1987

48. Lewitt RM, Muehllehner G, Karp JS: Three-dimensional image reconstruction for PET by multi-slice rebinning and axial image filtering. Phys Med Biol 39:321-339, 1994

49. Defrise M, Kinahan PE, Townsend DW, et al: Exact and approximate rebinning algorithms for 3D PET data. IEEE Trans Med Imaging 16:145-158, 1997

50. Zanzonico PB: Technical requirements for SPECT: equipment and quality control, in Kramer EL, Sanger JJ (eds): Clinical Applications in SPECT. New York, Raven Press, 1995, pp 7-41

51. Miller TR, Wallis JW: Fast maximum-likelihood reconstruction. J Nucl Med 33:1710-171, 1992

52. Miller TR, Wallis JW: Clinically important characteristics of maximum-likelihood reconstruction. J Nucl Med 33: 1678-1684, 1992

53. Hudson HM, Larkin RS: Accelerated image reconstruction using ordered subsets of projection data. IEEE Trans Med Imaging 13:601-609, 1994

54. Matej S, Lewitt RM: Practical considerations for 3-D image reconstruction using spherically symmetric volume elements. IEEE Trans Med Imaging 15:68-78, 1996

55. Matej S, Lewitt RM: Efficient 3D grids for image reconstruction using spherical-symmetric volume elements. IEEE Trans Nucl Sci 42:1361-1370, 1996

56. Daube-Witherspoon ME, Matej S, Karp JS, et al: Application of the 3D row action maximum likelihood algorithm to clinical PET imaging. IEEE Trans Nucl Sci 48:24-30, 2001

57. Hoffman EJ, Huang SC, Phelps ME: Quantitation in positron emission computed tomography: 1. Effect of object size. J Comput Assist Tomogr 3:299-308, 1979

58. Schoder H, Erdi Y, Larson S, et al: PET/CT: A new imaging technology in nuclear medicine. Eur J Nucl Med Mol 30:1419-1437, 2003

59. PET on display: Notes from the 59th SNM Annual Meeting. J Nucl Med (Newsline) 24N–26N, 2003

60. Kluetz PG, Meltzer CC, Villemagne VL, et al: Combined PET/CT Imaging in Oncology. Impact on Patient Management. Clin Positron Imaging 3:223-230, 2000

61. Ling CC, Humm J, Larson S, et al: Towards multidimensional radiotherapy (MD-CRT): biological imaging and biological conformality. Int J Radiat Oncol Biol Phys 47:551-560, 2000

62. Chatziioannou AF: PET scanners dedicated to molecular imaging of small animal models. Mol Imaging Biol 4:47-63, 2002

63. Del Guerra A, Belcari N: Advances in animal PET scanners. Q J Nucl Med 46:35-47, 2002

64. Herschman HR: Micro-PET imaging and small animal models of disease. Curr Opin Immunol 15:378-384, 2003

65. Jeavons AP: Small-animal PET cameras. J Nucl Med 41:1442-1443, 2000

66. Myers R: The biological application of small animal PET imaging. Nucl Med Biol 28:585-593, 2001

67. Myers R, Hume S: Small animal PET. Eur Neuropsychopharmacol 12:545-555, 2002

68. Tornai MP, Jaszczak RJ, Turkington TG, et al: Small-animal PET: advent of a new era of PET research. J Nucl Med 40:1176-1179, 1999

69. Chatziioannou AF, Cherry SR, Shao Y, et al: Performance evaluation of microPET: a high-resolution lutetium oxyorthosilicate PET scanner for animal imaging. J Nucl Med 40:1164-1175, 1999

70. Cherry SR, Shao Y, Silverman RW, et al: MicroPET: a high resolution PET scanner for imaging small animals. IEEE Trans Nucl Sci NS- 44:1161-1166, 1997

71. Tai C, Chatziioannou A, Siegel S, et al: Performance evaluation of the microPET P4: a PET system dedicated to animal imaging. Phys Med Biol 46:1845-1862, 2001

72. Motta A, Damiani C, Del Guerra A, et al: Use of a fast EM algorithm for 3D image reconstruction with the YAP-PET tomograph. Comput Med Imaging Graph 26:293-302, 2002

73. Jeavons A, Chandler RA, Dettmar CAR: A 3D HIDAC-PET camera with sub-millimetre resolution for imaging small animals. IEEE Trans Nucl Sci 46:468-473, 1999

74. Townsend D, Frey P, Jeavons A, et al: High density avalanche chamber (HIDAC) positron camera. J Nucl Med 28:1554-1562, 1987

75. Evans RD: The Atomic Nucleus. New York, McGraw-Hill, 1972, p 628